Influences of the Kuroshio/Oyashio Extensions on Air–Sea Heat Exchanges and Storm-Track Activity as Revealed in Regional Atmospheric Model Simulations for the 2003/04 Cold Season*

Bunmei Taguchi

Earth Simulator Center, JAMSTEC, Yokohama, Japan

Hisashi Nakamura

*Department of Earth and Planetary Science, University of Tokyo, Tokyo, and Research
Institute for Global Change, JAMSTEC, Yokohama, Japan*

Masami Nonaka

Research Institute for Global Change, JAMSTEC, Yokohama, Japan

Shang-Ping Xie

IPRC, and Department of Meteorology, SOEST, University of Hawaii at Manoa, Honolulu, Hawaii

(Manuscript received 30 October 2008, in final form 8 July 2009)

ABSTRACT

Influences of oceanic fronts in the Kuroshio and Oyashio Extension (KOE) region on the overlying atmosphere are investigated by comparing a pair of atmospheric regional model hindcast experiments for the 2003/04 cold season, one with the observed finescale frontal structures in sea surface temperature (SST) prescribed at the model lower boundary and the other with an artificially smoothed SST distribution. The comparison reveals the locally enhanced meridional gradient of turbulent fluxes of heat and moisture and surface air temperature (SAT) across the oceanic frontal zone, which favors the storm-track development both in winter and spring. Distinct seasonal dependency is found, however, in how dominantly the storm-track activity influences the time-mean distribution of the heat and moisture supply from the ocean.

In spring the mean surface sensible heat flux (SHF) is upward (downward) on the warmer (cooler) side of the subarctic SST front. This sharp cross-frontal contrast is a manifestation of intermittent heat release (cooling) induced by cool northerlies (warm southerlies) on the warmer (cooler) side of the front in association with migratory cyclones and anticyclones. The oceanic frontal zone is thus marked as both the largest variability in SHF and the cross-frontal sign reversal of the SHF skewness. The cross-frontal SHF contrasts in air–sea heat exchanges counteract poleward heat transport by those atmospheric eddies, to restore the sharp meridional gradient of SAT effectively for the recurrent development of atmospheric disturbances. Lacking this oceanic baroclinic adjustment associated with the SST front, the experiment with the smoothed SST distribution underestimates storm-track activity in the KOE region.

In winter the prevailing cold, dry continental airflow associated with the Asian winter monsoon induces a large amount of heat and moisture release even from the cooler ocean to the north of the frontal zone. The persistent advective effects of the monsoonal wind weaken the SAT gradient and smear out the sign reversal of the SHF skewness, leading to weaker influences of the oceanic fronts on the atmosphere in winter than in spring.

Corresponding author address: Bunmei Taguchi, Earth Simulator Center, Japan Agency for Marine–Earth Science and Technology, 3173-25 Showa-machi, Kanazawa-ku, Yokohama, Kanagawa 236-0001, Japan.
E-mail: bunmei@jamstec.go.jp

1. Introduction

The Kuroshio and Oyashio Extension (KOE) region is known as one of the major centers of action of decadal-scale variability in the extratropical ocean–atmosphere system over the North Pacific (Nakamura et al. 1997; Nakamura and Kazmin 2003; Schneider and Cornuelle 2005; Qiu et al. 2007; Kwon and Deser 2007). In this zonally elongated domain, the pronounced decadal-scale variability in sea surface temperature (SST) is caused largely by oceanic processes, including axial migration of local SST fronts (Xie et al. 2000; Seager et al. 2001; Nakamura and Kazmin 2003; Nonaka et al. 2006, 2008) in association with incoming wind-forced oceanic Rossby waves (Schneider and Miller 2001; Qiu 2003; Taguchi et al. 2007) and anomalous thermal advection by the Kuroshio and its extension (KE; Qiu 2000; Tomita et al. 2002; Vivier et al. 2002; Scott and Qiu 2003) and by the Oyashio and its subpolar extension (OE; Nonaka et al. 2008). Because they are caused by these oceanic processes rather than by local atmospheric forcing, those SST anomalies in the KOE region accompany surface turbulent heat fluxes that can act as a thermal forcing on the overlying atmosphere (Tanimoto et al. 2003; Nonaka et al. 2006). In fact, numerical experiments by Peng and Whitaker (1999) suggest that the SST anomaly in the KOE region may be able to force a basin-scale atmospheric response, although it may be sensitive to the background flow. Furthermore, observational evidence is emerging that the midlatitude atmosphere does respond to fine structures of SST associated with oceanic fronts and eddies (Nonaka and Xie 2003; Chelton et al. 2004; Xie 2004; Tokinaga et al. 2006; Small et al. 2008), but the response is localized and mostly confined to the atmospheric planetary boundary layer (PBL). Climatologically, a western boundary current associated with a subtropical gyre transports a huge amount of heat from the tropics into a midlatitude oceanic frontal zone, where the heat thus transported is intensively released into the atmosphere mostly in the cold season (e.g., Kelly and Dong 2004). Minobe et al. (2008) have demonstrated that intense heat release from the Gulf Stream enhances convective precipitation locally, suggesting that associated latent heat release may force a basin-scale atmospheric response, as postulated by Hoskins and Valdes (1990). Tokinaga et al. (2009) have synthesized in situ and satellite observations to show that clouds in winter tend to develop on the warmer flank of the KE reaching into the midtroposphere. Nevertheless, the extent to which the extratropical ocean–atmosphere interaction contributes to shaping the North Pacific climate and causing its decadal variability has not been fully understood, due to the lack of

consensus on how the atmosphere responds to extratropical SST anomalies (Kushnir et al. 2002).

Among studies that discussed the large-scale atmospheric influence of finescale oceanic fronts, Nakamura et al. (2004) proposed a new framework for interpreting how the mean state of the tropospheric general circulation is maintained, in which midlatitude oceanic fronts play a significant role in anchoring storm tracks and their associated westerly polar-front jets. They argued that the differential heat supply from the ocean to the atmosphere across a midlatitude oceanic frontal zone acts to maintain the surface baroclinicity, which is necessary for the recurrent development of cyclones and anticyclones to counteract their poleward heat transport. This effective restoration of baroclinicity is referred to as "oceanic baroclinic adjustment" by Nakamura et al. (2008), who have confirmed the anchoring effects of the frontal SST distribution on a storm track via idealized atmospheric general circulation model (AGCM) experiments with an "aquaplanet" setting with or without zonally uniform frontal SST structures. AGCM experiments by Inatsu et al. (2003) and Brayshaw et al. (2008) also confirmed the high sensitivity of storm-track activity to the midlatitude SST gradient. However, it has not been fully understood what specific processes are operative in the oceanic baroclinic adjustment.

Recently, Nonaka et al. (2009) have scrutinized the processes involved in the maintenance of surface baroclinicity across a prominent oceanic front simulated in a high-resolution coupled GCM. They focused on the Antarctic polar frontal zone (APFZ) in the southern Indian Ocean. The APFZ exhibits roughly a single frontal structure away from continents, which allows a fairly straightforward comparison with the aforementioned aquaplanet experiments. Focusing on the air–sea heat exchange in the coupled GCM, they found a large amount of sensible heat released from the ocean only on the warmer side of the APFZ under cold equatorward winds behind an atmospheric cold front. Migratory cyclones and anticyclones act to relax the meridional gradient of the surface air temperature (SAT) by advecting cold (warm) air equatorward (poleward) across the surface baroclinic zone along the oceanic front, but the differential oceanic heat supply across the oceanic front restores the cross-frontal SAT gradient effectively. The analysis shows that the process of the oceanic baroclinic adjustment (Nakamura et al. 2008) is operative along the model-simulated APFZ.

Concerning the North Pacific climate and its variability, it is of great interest to see to what extent the findings of Nonaka et al. (2009) are applicable to the KOE region, where the oceanic frontal zone exhibits a more complex structure than in the APFZ (Nonaka

et al. 2006). Furthermore, the air–sea heat and moisture exchanges are subject to the seasonally dependent influences of the adjacent Eurasian continent in the form of summer and winter monsoons. Another important scientific issue that remains unsolved is whether the zonally confined surface baroclinic zone in the KOE region can exert a significant impact on the mean storm-track activity. To address these issues, the present study investigates the influences of the oceanic fronts on surface heat fluxes and the overlying atmosphere in the KOE region by using a regional atmospheric model configured for the western and central portions of the North Pacific basin. The impacts of the oceanic fronts are assessed by comparing a pair of hindcast integrations for the 2003/04 cold season with and without the finescale frontal SST structures at the model lower boundary. Our model experiments for the KOE region with a realistic land–ocean configuration should complement the previous idealized aquaplanet model studies (Inatsu et al. 2003; Nakamura et al. 2008; Brayshaw et al. 2008) and a coupled GCM diagnosis for the APFZ (Nonaka et al. 2009), to deepen our understanding on the role of the midlatitude oceanic fronts in the climate system. We show that our regional model hindcast integration with the observed high-resolution SST field prescribed can reproduce surface turbulent heat fluxes and storm-track activity in a manner consistent with satellite-based heat flux analysis and an atmospheric reanalysis product. Our analysis reveals how the cross-frontal contrasts in surface heat fluxes act to maintain the surface baroclinicity to anchor the storm track along the KOE region both in winter and spring. It also reveals some distinct winter–spring contrasts in the spatiotemporal structure of the heat and moisture supply from the ocean.

The rest of the paper is organized as follows. Section 2 describes the model experiment and the observational data employed in this study. Section 3 briefly presents our model validation against the observations with respect to surface winds and turbulent heat fluxes. Sections 4 and 5 discuss the influences of oceanic fronts in the KOE region on the distribution of the surface sensible heat flux, near-surface baroclinicity, and storm-track activity. We discuss the role of moist processes in the storm-track activity in sections 6 and 7 presents a summary.

2. Model experiment and observational data

a. Model experiment

We use an atmospheric regional model based on hydrostatic primitive equations in spherical coordinates that has been developed by Y. Wang (Wang et al. 2003) of the International Pacific Research Center (IPRC), University of Hawaii. The model calculates surface heat fluxes at the ocean and land surfaces, using bulk formulas based on modified Monin–Obukhov similarity theory (Fairall et al. 2003). The vertical mixing is computed by a 1.5-level nonlocal turbulence closure scheme (Langland and Liou 1996). Parameterizations for radiation, subgrid-scale convection, grid-scale moist processes, and land surface processes are documented in Wang et al. (2005). The model has been utilized for studying the East Asian monsoon (Wang et al. 2003), the atmospheric response to tropical instability waves in the Pacific Ocean (Small et al. 2003), and PBL clouds associated with a subtropical anticyclone over the southeastern Pacific (Wang et al. 2005). For the present study, the model is configured for a domain that covers the western and central portions of the North Pacific basin (15°–70°N, 120°E–150°W). To resolve fine frontal-scale features in the SST field, the model resolution is set to be 0.5° in both latitude and longitude with 28 vertical sigma levels (including 11 levels below 800 hPa). The top of the model atmosphere is placed around the 15-hPa level.

A pair of model experiments has been conducted for the 7-month period from October 2003 to April 2004. In each of the integrations, 6-hourly fields of the zonal and meridional wind velocities, air temperatures, and relative humidities, based on the National Centers for the Environmental Prediction–National Center for the Atmospheric Research (NCEP–NCAR) reanalysis (Kalnay et al. 1996), were prescribed at the model lateral boundaries, in order to introduce realistic signals of synoptic-scale disturbances that come mainly from the upstream into the model interior. As the model lower-boundary condition for the control (CNTL) experiment, weekly mean SST fields based on measurements by the Advanced Microwave Scanning Radiometer (AMSR-E; Wentz and Meissner 2000) were interpolated linearly onto model time steps. With the resolution as high as 0.25° in both latitude and longitude, the SST fields specified at the model surface can well resolve the fine structures of the oceanic fronts and mesoscale eddies. During the 7-month period, the KE was in its stable path, maintaining a sharp SST front along it (Qiu and Chen 2005). In the other [smoothed (SMTH)] experiment, the SST fields had been exposed to 10° running means in the latitudinal direction before being assigned as the model boundary condition. The smoothing has eliminated the sharp SST gradients associated with the oceanic fronts.

Our experimental design, where the atmospheric model is integrated with prescribed SSTs, is equivalent to assuming that the ocean has infinite heat capacity or, equivalently, a very deep mixed layer. In the cold season this assumption appears to be valid for the KE region, where the mixed layer becomes as deep as 200 m in February and March, and it is still deeper than 100 m in

January and April based on recent observations using Argo floats (Kako and Kubota 2007). In addition, the strong advective effects of the Kuroshio and Oyashio also contribute positively to the persistency of SSTs in the KOE region. Our model experiments are thus aimed at highlighting the ocean-to-atmosphere influences in the cold season when SSTs are almost persistent against heat exchanges with the atmosphere. Though not fully addressing the whole air–sea coupled processes, our experiments will be instructive in deepening our understanding of how the midlatitude atmosphere responds to the thermal influence by the ocean.

Our model integrations include the period of shipboard atmospheric sounding surveys over the KOE region (Tokinaga et al. 2006). A preliminary comparison shows that the CNTL experiment simulates well the observed dependence of the vertical structure of the PBL upon the near-surface static stability (Taguchi 2006). In the present study, the simulated fields are analyzed, with particular emphasis on the surface heat fluxes, near-surface baroclinicity, and storm-track activity.

b. Observations

The regional model CNTL experiment is compared with the following observational data. We use a gridded dataset of turbulent sensible and latent heat fluxes (hereafter abbreviated as SHF and LHF, respectively) at the ocean surface taken from the Japanese Ocean Flux datasets with Use of Remote Sensing Observations version 2 (J-OFURO2; Kubota and Tomita 2007). In the J-OFURO2 dataset, those fluxes have been constructed from high-resolution SST and ocean surface meteorological data estimated from multiple satellites and in situ observations using the bulk formula (Fairall et al. 2003). The daily mean product optimally interpolated onto a regular $1.0° \times 1.0°$ latitude–longitude grid is available on the J-OFURO2 Web site (http://dtsv.scc.utokai.ac.jp/). The simulated fields of wind and temperature are compared with the Japanese 25-year Reanalysis Project (JRA-25) of the global atmosphere (Onogi et al. 2007), and the precipitation rate is compared with the Global Precipitation Climatology Project (GPCP) merged precipitation product (Huffman et al. 2001). Statistics for representing local storm-track activity have been constructed as in Nakamura et al. (2002).

3. Month-to-month changes in surface wind and turbulent heat fluxes

In this section, we briefly present a comparison of month-to-month changes in surface wind and seasonal surface turbulent heat fluxes between the CNTL experiment and the observations, so that the reader can get an overview of the marine meteorological features characteristic of the KOE region before discussing our more detailed analyses in the following sections. The corresponding comparisons of other simulated quantities, including precipitation and meridional eddy heat transport, are discussed in later sections.

a. Surface winds

Figure 1 compares simulated monthly mean fields of surface wind[1] at 10-m height based on daily mean output from the CNTL experiment with those from the JRA-25 analysis for December 2003 and January, March, and April 2004. For a straightforward comparison with the model variables for which only the daily mean fields are available, the 6-hourly JRA-25 surface wind velocities were first averaged into a daily mean, from which the daily wind speeds were evaluated. The daily mean wind speeds from the model and the observations were then averaged in the same manner to produce their monthly means. During the 2003/04 cold season, month-to-month changes in surface winds based on the JRA-25 analysis are characterized by the rapid maturing of the East Asian winter monsoon in December and its subsequent gradual weakening in late winter and early spring (Fig. 1). Specifically, there was no prevailing wind direction in November (not shown) around Japan, until the strong monsoonal northwesterly or westerly winds started to prevail in early December (Fig. 1a) and persisted until late February (Fig. 1b) over the Japan Sea and the western North Pacific off the coast of Japan. In March and April (Figs. 1c and 1d), the mean surface wind speed diminished, while the meridional component turned southerly. Overall, the surface wind fields simulated in the CNTL experiment capture the observed seasonal transition as mentioned above, except that the surface wind speeds tend to be slightly underestimated and the termination of the winter monsoon is simulated in early February. Nevertheless, the model can reproduce the contrasting features in the mean wind speed and prevailing wind direction between the winter (December–January) and spring (March–April). The former regime is characterized by the persistent monsoonal winds, whereas the latter is marked by the frequent passage of migratory cyclones and anticyclones and thus by highly variable wind directions.

b. Surface heat fluxes

Figures 2 and 3 compare the seasonal-mean fields of surface SHF and LHF, respectively, between the CNTL

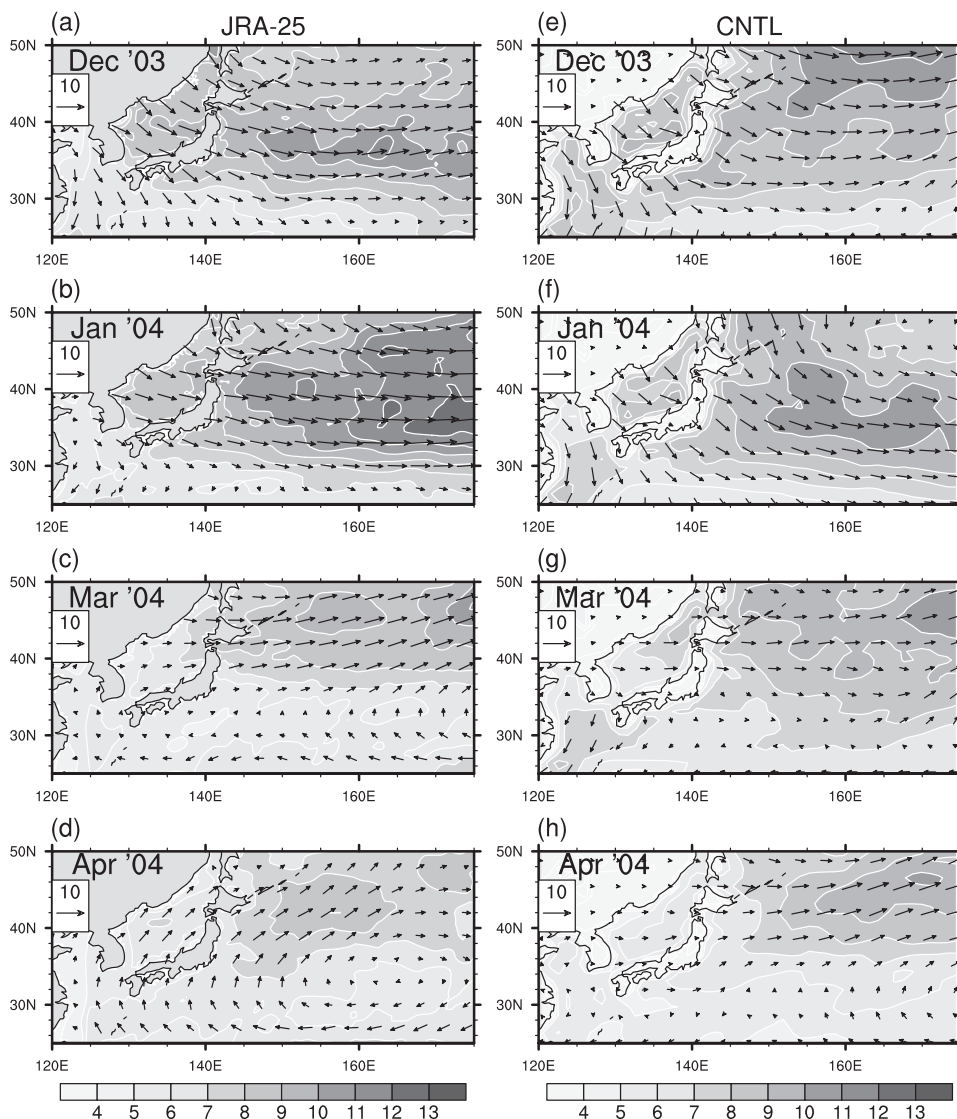[1] Hereafter, "surface wind" denotes wind at 10 m above the surface.

FIG. 1. Monthly mean surface wind vector [arrows; scaling (m s^{-1}) near the upper-left corner] and its speed (shading as indicated at the bottom), based on (a)–(d) the JRA-25 reanalysis and (e)–(h) the model CNTL experiment for December 2003 and January, March, and April 2004, as indicated. Units are in m s^{-1}. Note that the monthly mean wind velocity and speed are computed from daily mean fields both for the model and the reanalysis.

experiment and the J-OFURO2 analysis. Focusing on two distinct wind regimes described above, the comparison is made separately for the midwinter and early spring periods (hereafter simply referred to as the winter and spring seasons, respectively), corresponding to periods from 1 December 2003 to 15 January 2004 and from 16 March to 30 April 2004, respectively. Reflecting the seasonal transition of the surface winds associated with the evolution of the East Asian winter monsoon, the analyzed fluxes exhibit marked seasonal changes over the western North Pacific. The heat and moisture release from the ocean was moderate in November 2003

(not shown). Once the East Asian winter monsoon emerges in December, both SHF and LHF increased sharply over the extensive maritime region around Japan and the KOE region, owing to the frequent and sometimes persistent outbreaks of dry, cold continental air onto the relatively warm ocean. Under the prevailing monsoonal airflow in winter, SHF was strongest over the Sea of Japan, the zonally elongated region along the Kuroshio south of Japan and the KE, and the mixed water region between the KE and OE (Fig. 2a). In the corresponding distribution of LHF (Fig. 3a), the peak over the Sea of Japan was weaker, while another peak along the Kuroshio
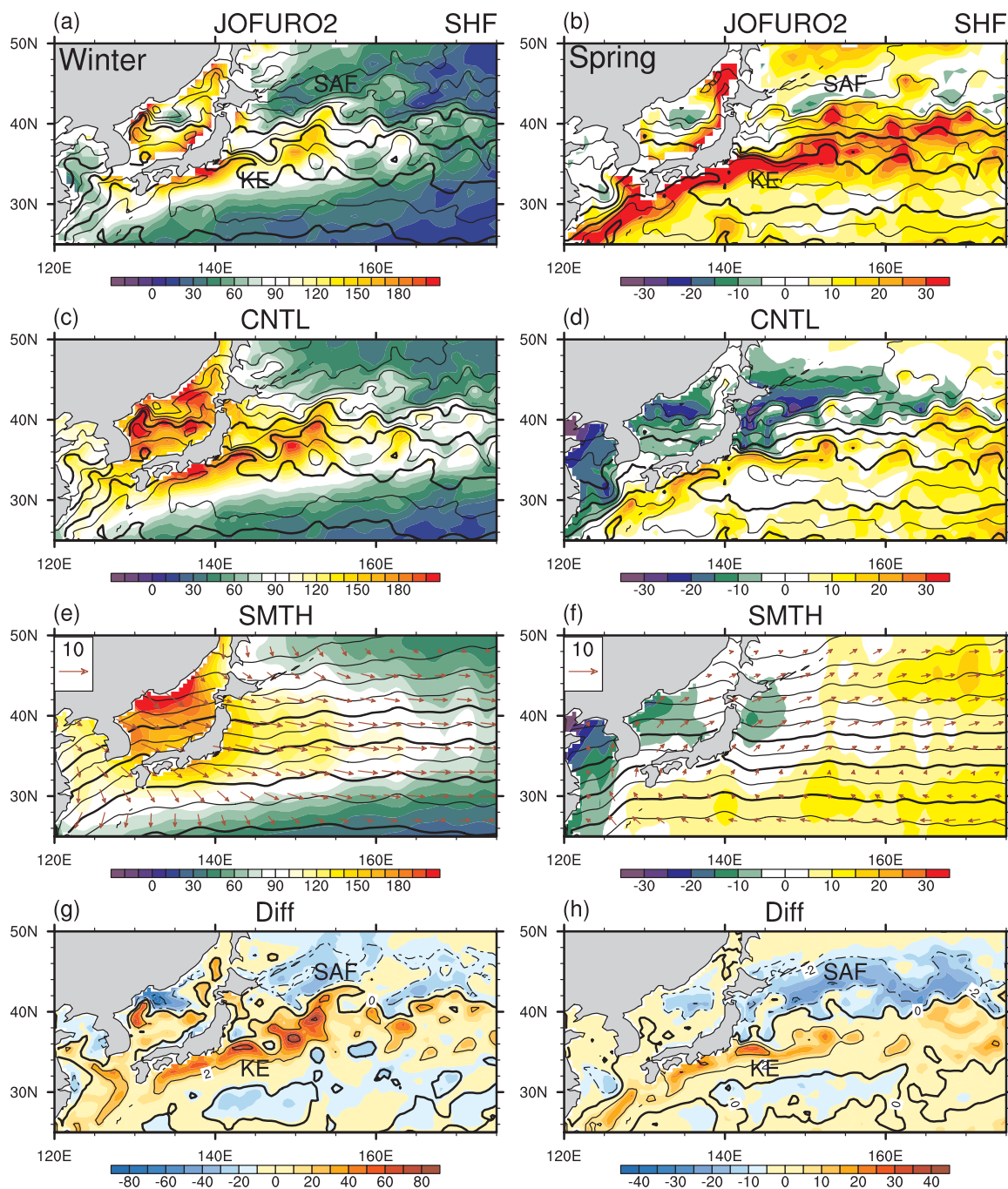
FIG. 2. Seasonal-mean surface SHF (W m^{-2}; color shading as indicated at the bottom) based on the (a),(b) JOFURO analysis, and the (c),(d) CNTL and (e),(f) SMTH experiments. The prescribed SST field is superposed with black contours with intervals of 2°C, and the contours for 12°, 16°, 20°, and 24°C are thickened. In (a),(b) and (g),(h), approximate locations of the KE and the subarctic fronts are labeled with ''KE'' and ''SAF'', respectively. In (e),(f), mean surface wind vectors (m s^{-1}) based on the SMTH experiment are also superposed with red arrows. (g),(h) Difference in SHF (W m^{-2}; color shading as indicated at the bottom) between the two experiments (CNTL–SMTH). Left and right panels are for the winter season (from 1 Dec 2003 to 15 Jan 2004) and the spring season (from 16 Mar to 30 Apr 2004), respectively. Note that the scaling for the color shading differs between the seasons.
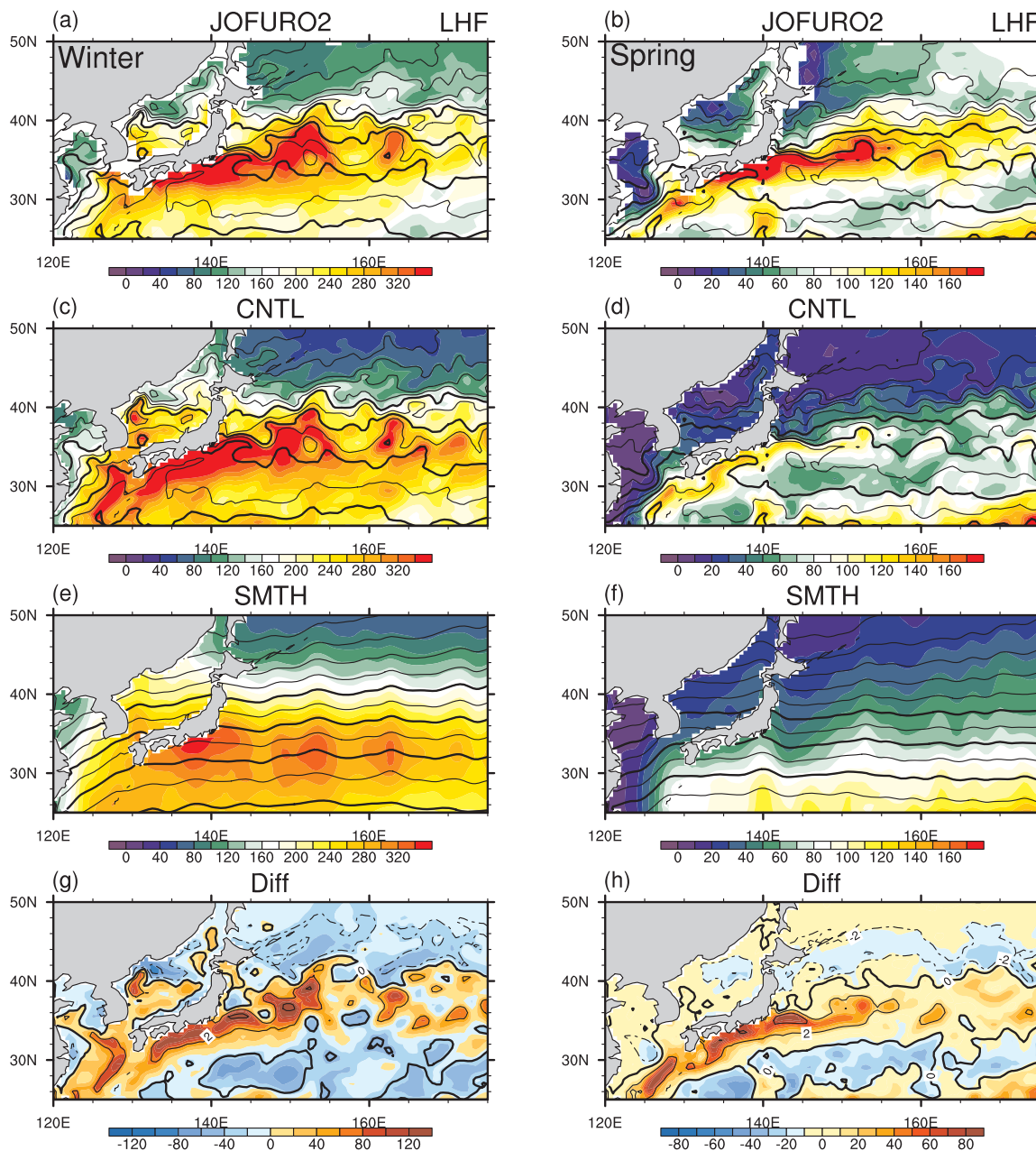
FIG. 3. Same as in Fig. 2 but for the surface LHF.

and KE was predominant. The distinctive spatial patterns between the SHF and LHF reflect the spatial dependence of the Bowen ratio that is sensitive to SST through nonlinearity in the Clausis–Clapeyron equation. The ratio is particularly low over the warm surface of the Kuroshio and KE, where the saturated vapor pressure is particularly high. Their distinction also reflects thermal adjustment processes of the cold monsoonal air mass through its heat exchanges with the underlying warmer ocean surface. In winter, the air–sea

temperature difference (SST − SAT) exceeded 20°C over the western portion of the Sea of Japan but it was reduced to about 10°C south of Japan. As the winter monsoon decayed, the heat release from the ocean gradually decreased in March 2004 (Figs. 2b and 3b).

Overall, the CNTL experiment captures the aforementioned seasonal dependence of the analyzed surface heat fluxes (Figs. 2a–d and 3a–d). The reproducibility is reasonable in winter, except for a slight overestimation of SHF in the model over the Sea of Japan and an underestimation

of LHF north of the subarctic front (SAF) along ~44°N. Meanwhile, the model underestimates the J-OFURO2 heat fluxes over the KOE region perhaps due to the underestimated storm-track activity in spring. Nevertheless, the model captures the augmented SHF and LHF along the Kuroshio south of Japan and along the KE.

4. Signature of oceanic fronts in the sensible heat flux distribution

In this section, we assess the influence of the Kuroshio and Oyashio Extensions on SHF statistics by comparing the CNTL and SMTH experiments separately for the winter and spring seasons defined above.

a. Winter monsoon influence on SHF and its intensification along oceanic fronts

As is apparent in Figs. 2c and 2e, the large-scale SHF distribution in winter is reproduced both in the CNTL and SMTH experiments. Over the Sea of Japan, upward SHF as large as 180 W m^{-2} is simulated, owing to recurrent outbreaks of cold continental air by the northwesterly monsoonal winds (Fig. 2e) onto the relatively warm ocean surface. In the SMTH experiment, a monotonic downwind reduction of SHF is attributable to the thermal adjustment of the continental airmass with heat supply from the underlying ocean (Ninomiya et al. 2006), manifested as the corresponding reduction in SST − SAT[2] (Fig. 4c). The CNTL experiment also simulates finer features (Fig. 2c). The most distinct feature is the locally augmented SHF along the Kuroshio and KE, where a continental air mass that has been modified over the Sea of Japan encounters the warmer sea surface. The SST − SAT difference is thus as large as that over the Sea of Japan (Fig. 4a), leading to comparably strong SHFs over the two maritime regions.

By the spring period the monsoonal northwesterly has ceased, and the mean surface wind has turned southerly over the marginal seas (Fig. 2f), yielding weak downward time-mean SHFs (Figs. 2d and 2f). Compared to the winter situation, the surface wind becomes more variable in the spring associated with frequent passages of synoptic-scale disturbances. Though somewhat underestimated (Fig. 2b), the local enhancement of SHF along the Kuroshio and KE and its sharp decline to the north are reproduced (Fig. 2d) in the CNTL experiment but not in the SMTH experiment.

The aforementioned local confinement and intensification of SHFs are highlighted in the difference fields between the CNTL and SMTH experiments (Figs. 2g

and 2h). In the CNTL experiment, SHF is augmented by as much as 60 (30) W m^{-2} in the winter (spring) season along the Kuroshio axis south of Japan and along the KE off the east coast of Japan. In winter the SHF augmentation is also evident at ~40°N, just south of the subarctic oceanic front along the OE. As shown in Fig. 4, this frontal signature in SHF corresponds well with the difference between those experiments in near-surface static stability as measured by SST − SAT. Fundamentally, thermal advection associated with the wintertime monsoonal winds or springtime synoptic disturbances defines a large-scale SAT pattern at a particular instance. The tight gradient in near-surface static stability and SHF must be due to the corresponding gradient in SST across the oceanic fronts (Figs. 2 and 4).

b. Confinement of SHF variance to the oceanic fronts

The oceanic frontal signature in SHF can be seen not only in its seasonal mean but also in its subseasonal variability, which is defined as its local standard deviation estimated for the individual seasons. The subseasonal variability in SHF is enhanced within a zonal belt in the vicinity of the oceanic frontal zone east of Japan for both seasons (not shown). The effects of the oceanic frontal zone are depicted in detail in Fig. 5, which shows latitudinal profiles at 150°E of SHF statistics, including its seasonal mean, standard deviation, and skewness, in addition to the meridional gradients of SST and SAT. In each of the seasons, the observed profile of the SAT gradient (Figs. 5b and 5g) closely follows that of the SST gradient that attains its maximum at the SST fronts (Figs. 5a and 5f). Generally, however, the SAT gradient is slightly weaker than the SST gradient owing to the effects of poleward heat transport by atmospheric motion. Though somewhat overestimated, the seasonal mean and standard deviation of the wintertime SHF simulated in the CNTL experiment show fairly good agreement with those analyzed in the J-OFURO2 data, especially with respect to the positions of their peaks (Fig. 5d). The winter-mean SHF peaks just south of the oceanic frontal zone located between 38° and 41°N, reaching nearly 200 W m^{-2} under the persistent winter monsoon. A comparison of the mean and standard deviation of SHF between the CNTL and SMTH experiments confirms an imprint of the oceanic frontal zone on the SHF statistics (Fig. 5d). Relative to the SMTH experiment, the mean and standard deviation of the wintertime SHF both increase by ~60% at 37°N, just south of the frontal zone, where SST − SAT is enhanced (Fig. 5c) in the presence of the frontal SST gradient.

A similar impact of the oceanic frontal zone on the mean and standard deviation of SHF can be found in

---

[2] Hereafter, SAT denotes air temperature at 2 m above the surface.
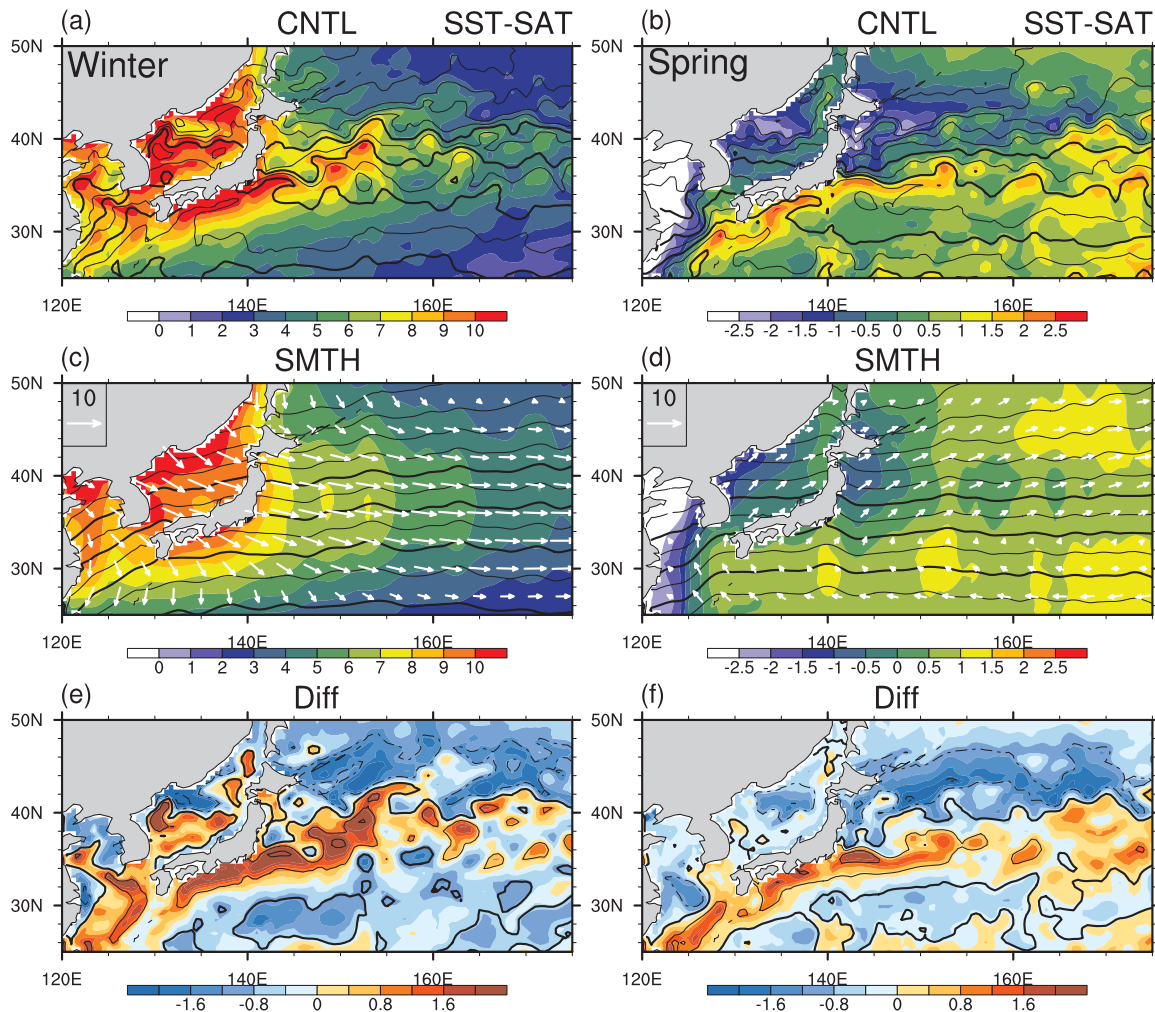
FIG. 4. Seasonal-mean near-surface static stability measured by SST − SAT (°C; color shading as indicated at the bottom) based on the (a),(b) CNTL and (c),(d) SMTH experiments. The prescribed SST field is superposed with black contours with intervals of 2°C, and the contours for 12°, 16°, 20°, and 24°C are thickened. In (c),(d), mean surface wind vectors (m s^{-1}) based on the SMTH experiment are also superposed with red arrows. (e),(f) Difference in SST − SAT (°C; color shading as indicated at the bottom) between the two experiments (CNTL–SMTH). Left and right panels are for the winter season (from 1 Dec 2003 to 15 Jan 2004) and the spring season (from 16 Mar to 30 Apr 2004), respectively.

spring. Reflecting the seasonal transition from the winter monsoon regime to the spring regime of frequent passage of synoptic disturbances, however, the standard deviation associated with the subseasonal variability[3] well exceeds the seasonal-mean SHF. As confirmed in the J-OFURO2 data, the spring-mean SHF in the CNTL experiment decreases sharply from positive to negative poleward across the subarctic front along the OE at 41°N (Fig. 5i). In contrast, no such sharp poleward decline of SHF is simulated in the SMTH experiment. Since SST declines sharply across the front, positive

(negative) SST − SAT values occur mostly to the south (north) of the subarctic front, yielding the cross-frontal sign reversal in the spring-mean SHF. As discussed in section 5b, the stronger seasonal mean and subseasonal variability in SHF in the CNTL experiment are also contributed by the enhanced storm-track activity relative to the SMTH experiment.

c. Contrasting skewness across oceanic fronts

Another intriguing SHF statistic is the skewness, a measure of the asymmetry of the subseasonal fluctuations about the time mean, which is defined as

$$\frac{\overline{\mathrm{SHF}'^3}}{\left(\overline{\mathrm{SHF}'^2}\right)^{3/2}},$$

---

[3] The subseasonal variability of SHF is mostly contributed by synoptic variability both in winter and spring.
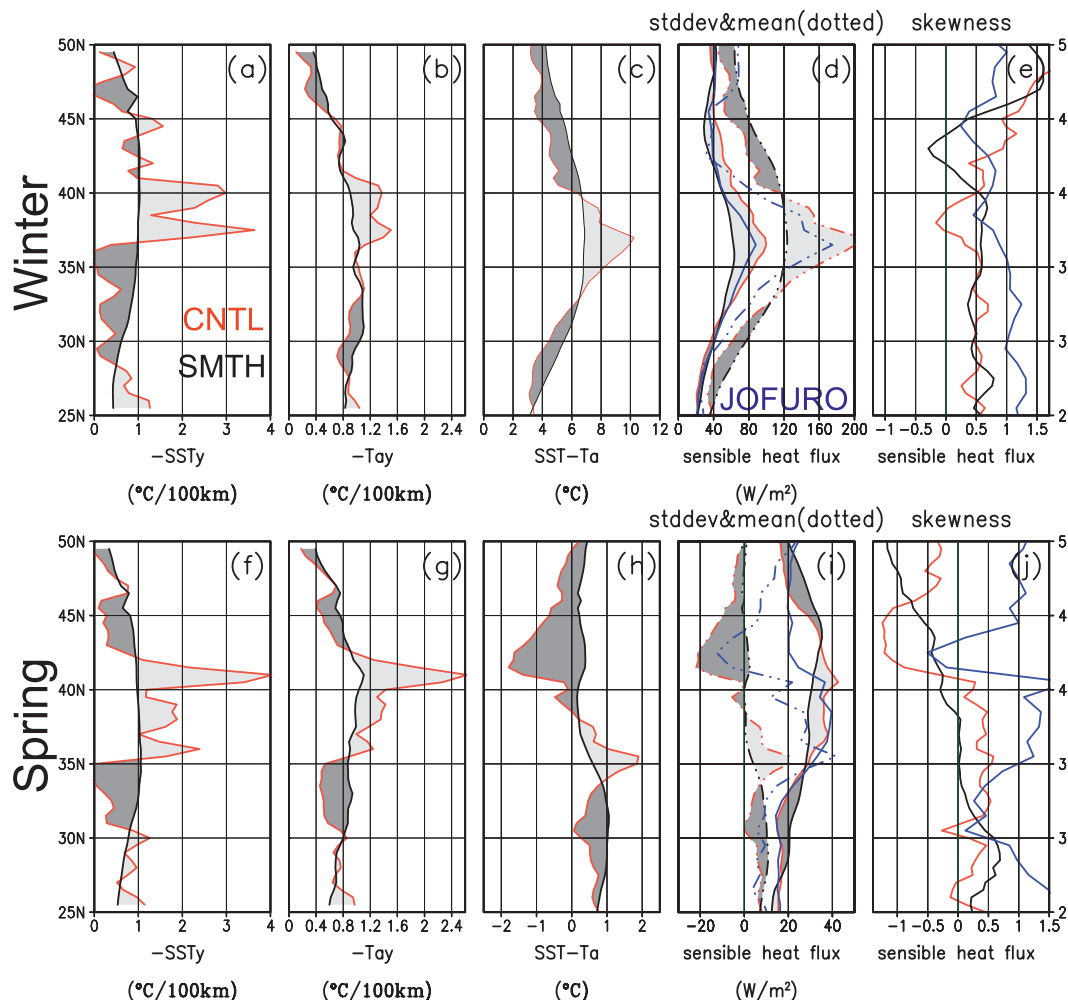
FIG. 5. Latitudinal profiles for 150°E of the meridional gradient of time-mean (a) SST and (b) SAT for winter; (c) the time mean SST − SAT; and the corresponding profiles of (d) time average (dotted lines), standard deviation (solid lines), and (e) skewness of SHF. (f)–(j) Same as in (a)–(e), respectively, but for spring. Red and black lines signify the CNTL and SMTH experiments, respectively, while blue lines denote the J-OFURO2 analysis. The positive (negative) differences between the CNTL and SMTH experiments are indicated with light and heavy shading, respectively, for the time-mean gradient of (a),(f) SST and (b),(g) SAT, and (c),(h) the time-mean SST − SAT and (d),(i) the mean and standard deviation of SHF.

where the overbar denotes the seasonal averaging and the prime subseasonal fluctuations. In a general meteorological circumstance, significant skewness is observed for a variable whose distribution is characterized by a zone of its tight meridional gradient (Nakamura and Wallace 1991), and SHF in the vicinity of an SST front is such a variable. As is evident in Figs. 5e,j, the skewness of SHF at 150°E exhibits a sharp contrast in its meridional distribution between winter and spring. In spring, both the CNTL experiment and J-OFURO2 analysis display a sharp sign reversal across the subarctic front at 41°N, with positive skewness to the south and negative skewness to the north. In contrast, the sign reversal is much more gradual in the SMTH experiment, where no

sharp SST front is prescribed in the model. Furthermore, no such apparent sign reversal of the SHF skewness across the oceanic frontal zone occurs in winter either in the CNTL or SMTH experiments or in the J-OFURO2 analysis.

To understand the characteristics of the cross-frontal jump in the SHF skewness, we inspect the latitude–time sections of SHF, SAT, and the surface wind plotted for 150°E in Fig. 6 separately for winter and spring based on the CNTL experiment. In both seasons, the instantaneous SHF was confined to a latitudinal band (35°–45°N) around the oceanic frontal zone. However, its spatiotemporal characteristics are contrasting between the two seasons. In spring, the SHF altered its sign recurrently
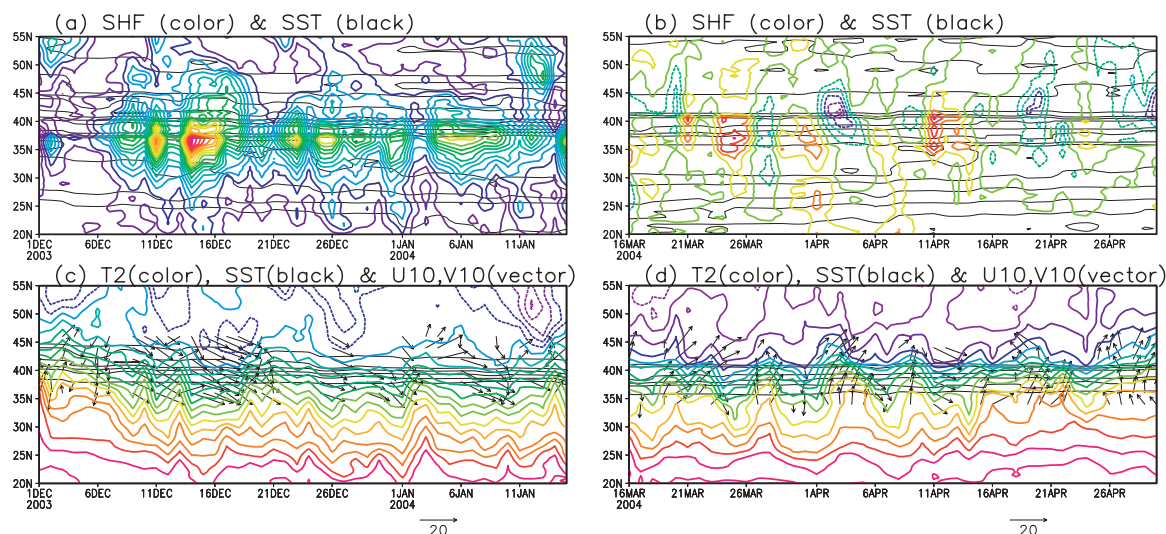
FIG. 6. Latitude–time sections for 150°E of (a) surface SHF (color contours with interval of 25 W m^{-2}), (c) SAT (color contours with intervals of 2°C) and surface wind vectors (scaling, in m s^{-1}, at the bottom) simulated in the CNTL experiment for winter. (b),(d) Same as in (a),(c), respectively, but for spring. Wind vectors are only plotted when the meridional component is stronger than 4 m s^{-1} between 35° (33°) N and 46° (44°) N in winter (spring). SST is superimposed with black contours (every 2°C), but only between 6° and 16°C in (c),(d).

with intervals of a few days. To the north of the front at 41°N, negative values of SHF were stronger and more frequent than positive values, while the opposite was the case to the south of the front (Fig. 6b). These spatiotemporal characteristics were caused by the recurrent passage of synoptic disturbances, which yielded day-to-day fluctuations in the meridional wind velocity and SAT (Fig. 6d). The fluctuations are strongest along the subarctic frontal zone, not only because the time-mean SAT gradient is strongest (Fig. 5g) but also because the storm track is collocated with the oceanic frontal zone (see Fig. 9). It should be stressed that the modest positive (negative) spring-mean SHF on the warmer (cooler) side of the SST front is a manifestation of the residual after the overall cancellation between the accumulated positive SHF under the northerlies and negative SHF under the southerlies. Those wind fluctuations are associated primarily with migratory cyclones and anticyclones but not with the seasonal mean wind field. Once cold air advected by northwesterly winds crosses the SST front, it augments SST − SAT and thus a large amount of sensible heat is released from the ocean primarily on the warmer side of the front (Fig. 6b). Meanwhile, upon crossing the SST front, warm air advected by southerlies turns SST − SAT negative on the cooler side of the SST front to yield downward (i.e., negative) SHF. As shown in frequency histograms of springtime SHF at 150°E based on separate samplings within 3° latitudinal segments to the south and north of the subarctic front (Fig. 7b), the frequency distribution is skewed about the mean SHF in the opposing manner across the front,

which is consistent with the cross-frontal sign reversal of the skewness. The northerly induced large sensible heat release from the ocean (SHF > 30 W m^{-2}) on the warmer side of the front is about twice as frequent as on its cooler side, whereas large sensible heat gain by the ocean (SHF ≤ 60 W m^{-2}) associated with southerlies is more frequent on its cooler side. Specifically, ~75% (85%) of the total positive (negative) SHF on the warmer (cooler) side of SST front is accumulated during those periods in which the northerly (southerly) component of the surface wind is stronger than 1.8 (7.8) m s^{-1} (i.e., deviations from the mean meridional velocity greater than a unit standard deviation), which occupy only 17% (20%) of the entire duration of the 45-day spring period. These statistics indicate the particular importance of transient eddies in the springtime air–sea heat exchanges around the subarctic frontal zone. Very similar statistics are found in SHF around the oceanic frontal zone over the southern Indian Ocean reproduced in a high-resolution coupled GCM (CGCM; Nonaka et al. 2009).

The corresponding histograms for winter (Fig. 7a) further elucidate the seasonal contrast in the SHF characteristics around the oceanic front. Under the persistent monsoonal northwerlies (Fig. 6c), the associated cold-air advection induces heat release from the ocean most of the time (Fig. 7a), with the seasonal mean SHF substantially greater on the warmer side of the oceanic front than on its cooler side. The wintertime SHF skewness is positive on both sides of the front, since SST − SAT and the surface wind speed both undergo particularly
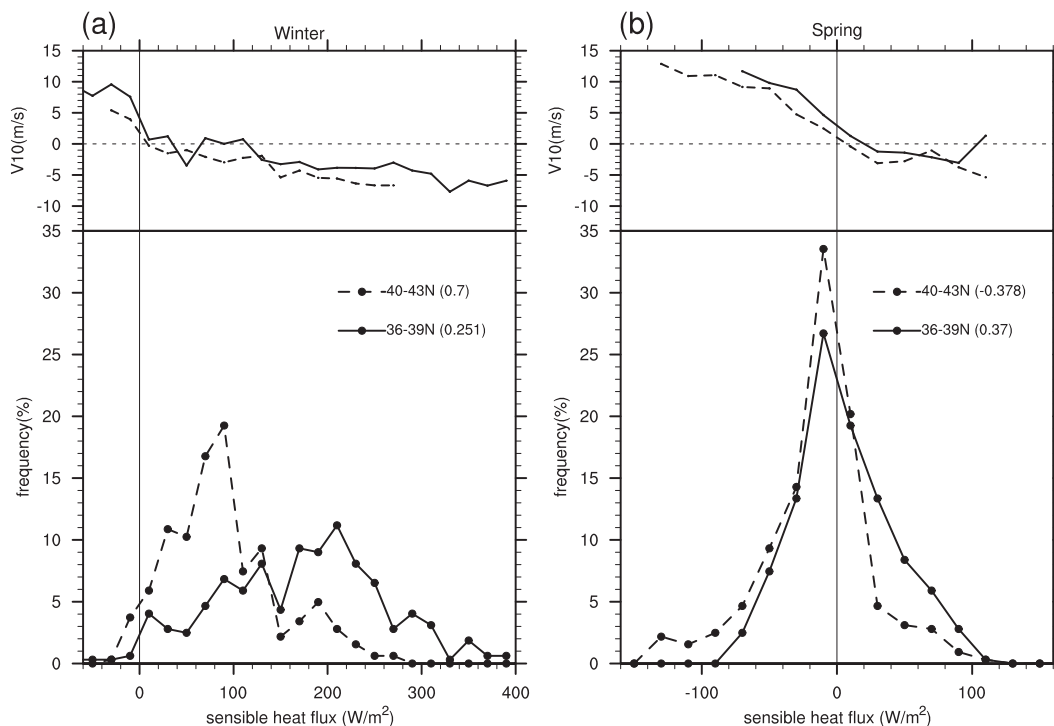
FIG. 7. Frequency histograms of daily SHF at 150°E to the south (36°~39°N; solid) and north (40°~43°N; dashed) of the subarctic front simulated in the CNTL experiment for (a) winter and (b) spring. The frequency is counted for bins with intervals of 20 W m^{-2}, for each of which the surface meridional wind velocity averaged over the samples is shown on top of the histograms. The skewness of SHF is indicated in parentheses separately to the south and north of the front.

large deviations from their wintertime means only during several events of extreme cold air on either side of the front (Figs. 6a and 6c). The confinement of instantaneous SHF to a narrow oceanic frontal zone and its asymmetry with respect to the oceanic front observed and simulated on either side of the SST front in spring are consistent with the analysis by Nonaka et al. (2009) for a prominent subpolar oceanic front in the southern Indian Ocean, while the strong influence of the East Asian winter monsoon on the spatiotemporal characteristics of SHF is a unique feature in the KOE region.

5. Surface baroclinicity and storm-track activity

a. Surface baroclinicity

In this section we discuss how the spatiotemporal structure of SHF discussed in the preceding section can influence the overlying atmosphere, focusing on the meridional SAT gradient that is important for storm development. In both spring and winter the meridional SAT gradient is augmented in the CNTL experiment (Figs. 8a and 8b) compared to the SMTH experiment (Figs. 8c and 8d). The augmentation is particularly large along individual oceanic fronts, most of which are lo-

cated within a KOE region bounded by the KE front to the south and the subarctic front to the north (Yasuda et al. 1996). As hinted in Figs. 2g and 2h, the meridional gradient in the seasonal-mean SHF is enhanced locally along those fronts, acting to maintain a local SAT gradient. In fact, Fig. 9 indicates that the zonally averaged (145E°~180°) meridional SAT gradient in the CNTL experiment is strongest in the surface baroclinic zone along the oceanic frontal zone (39°~43°N) for both winter and spring (Figs. 9b and 9f), corresponding to a maximum SST gradient of about 1.5 K (100 km)$^{-1}$ (Figs. 9a and 9e). In contrast, no such well-defined surface baroclinic zone is formed in the SMTH experiment.

Figures 8 and 9 show that the frontal enhancement in the local SAT gradient in the CNTL experiment relative to the SMTH experiment is larger in spring, especially along the subarctic frontal zone around 40°~44°N. In spring the peak SAT gradient [~1.35 K (100 km)$^{-1}$; Fig. 9f] reaches 90% of the underlying SST gradient [~1.5 K (100 km)$^{-1}$; Fig. 9e]. In winter the peak SAT gradient [~1.2 K (100 km)$^{-1}$; Fig. 9b] is weaker in spite of having the same strength as the underlying SST gradient in spring and a stronger cross-frontal mean SHF gradient [~10 W m^{-2} (100 km)$^{-1}$; Figs. 2c and 5d] than

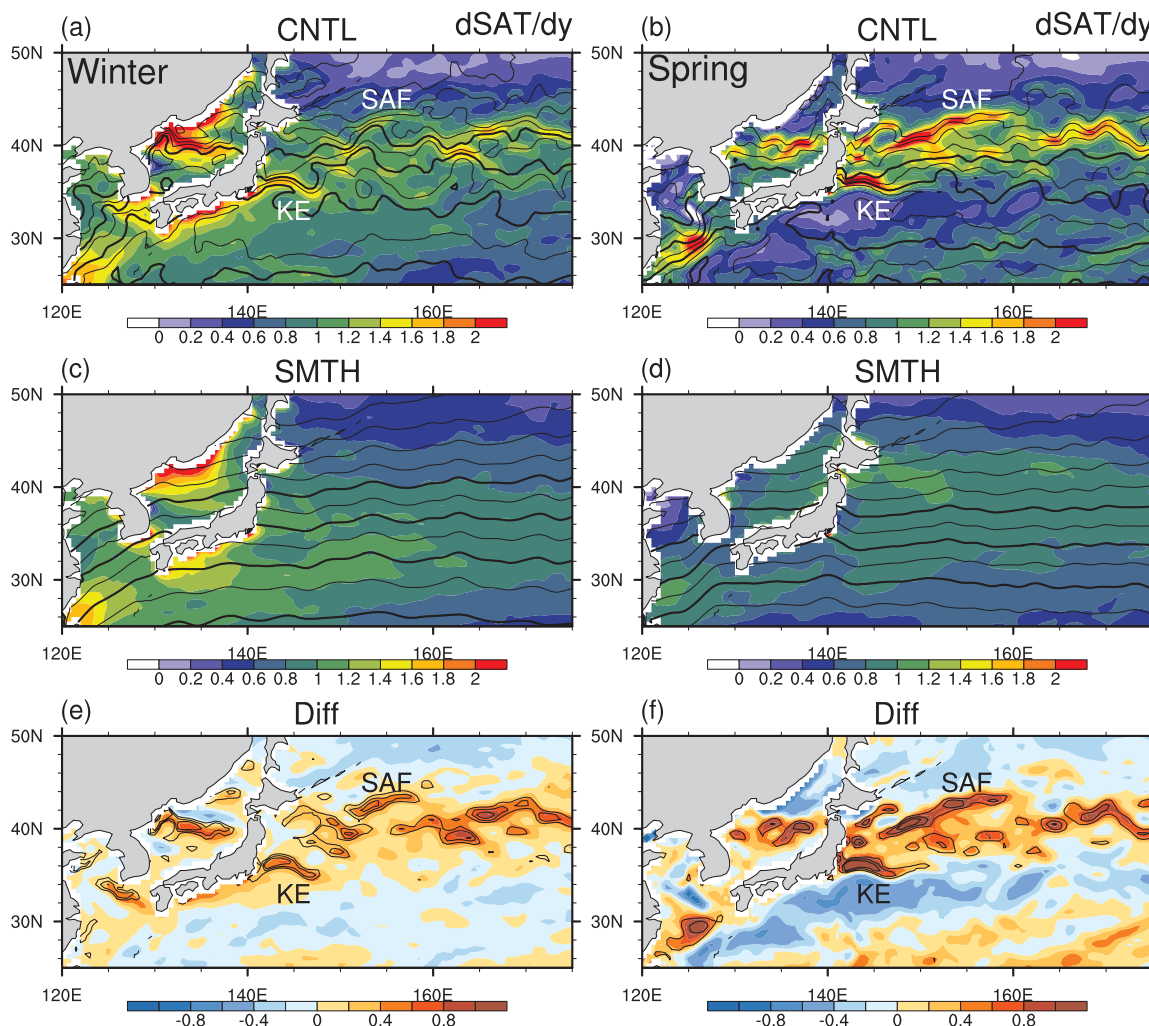FIG. 8. Meridional gradients of seasonal-mean SAT [color shading as indicated at the bottom, °C $(100 \text{ km})^{-1}$] based on the (a),(b) CNTL and (c),(d) SMTH experiments. The prescribed SST field is superposed with black contours with intervals of 2°C, and the contours for 12°, 16°, 20°, and 24°C are thickened. (e),(f) Difference in the meridional gradient of the mean SAT [color shading as indicated at the bottom, in °C $(100 \text{ km})^{-1}$] between the two experiments (CNTL–SMTH). Mean meridional SST gradients assigned in the CNTL experiment are superposed with black contours for 2, 3, 4°C $(100 \text{ km})^{-1}$. Left and right panels are for the winter season (from 1 Dec 2003 to 15 Jan 2004) and the spring season (from 16 Mar to 30 Apr 2004), respectively. In (a),(b) and (e),(f), the approximate locations of the KE and the subarctic fronts are labeled KE and SAF, respectively.

in spring [~3 W m^{-2} $(100 \text{ km})^{-1}$; Figs. 2d and 5i]. The stronger surface baroclinicity in spring thus cannot be explained solely by the time-mean SHF gradient but may be attributed to the effective restoring of the SAT gradient toward the local SST gradient via temporarily enhanced SHF contrasts across the oceanic frontal zone with frequent passages of weather systems (Nakamura et al. 2004, 2008; Nonaka et al. 2009). This restoration is manifested as the positive (negative) SHF skewness on the warmer (cooler) side of the frontal zone (Figs. 5–7). Through their analysis of high-resolution CGCM output, Nonaka et al. (2009) estimated that this restoring process through enhanced SHF associated with the pas-

sages of individual synoptic disturbances is quite efficient with a typical time scale of about 1 day. In spring, mean cross-frontal winds are weak in the KOE region, as in the case of the southern Indian Ocean frontal zone analyzed by Nonaka et al. (2009). Following their method, we estimate the restoration time scale in the KOE region in spring. Under the assumption that the air temperature (Ta) is uniform in the mixed layer, the time rate of change in the air–sea temperature difference (Ts − Ta) that would occur due solely to SHF may be written as follows:

$$\frac{\partial}{\partial t}(\text{Ta} - \text{Ts}) = -\frac{1}{\tau}(\text{Ta} - \text{Ts}).$$
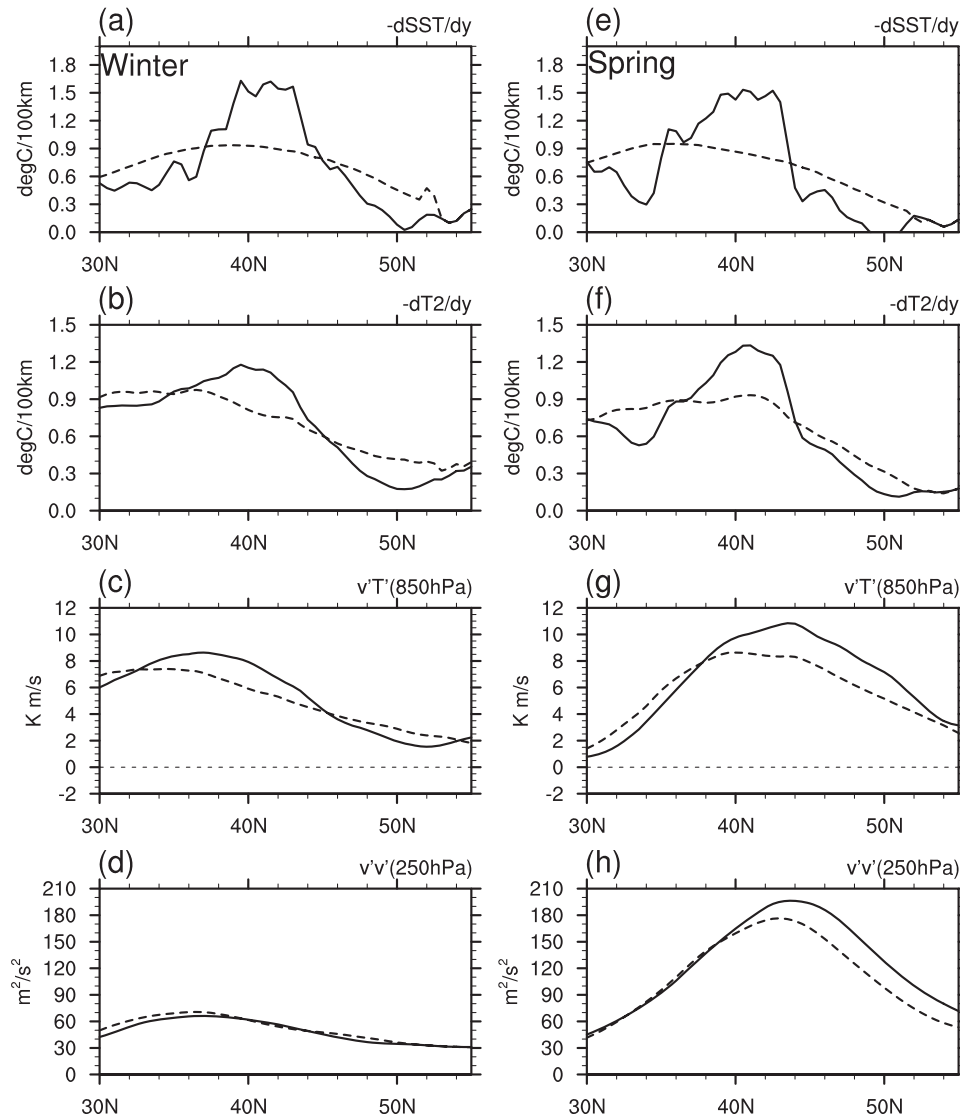
FIG. 9. Meridional profiles of the winter-mean meridional gradient [°C (100 km)$^{-1}$] of (a) SST and (b) SAT, and the corresponding profiles representing the activity of the synoptic disturbances measured as (c) the 850-hPa poleward heat flux $\overline{v'T'}$ (K m s^{-1}) and (d) the variance of the 250-hPa meridional wind velocity v'^2 (m^2 s^{-2}), based on longitudinal averaging for 145°E~180° in the CNTL (solid) and SMTH (dashed) experiments. (e)–(h) Same as in (a)–(d), respectively, but for spring.

Here, the restoration time scale τ is given by $\tau = C_p\rho H/\alpha$, with ρ the air density, H the mixed layer depth, C_p the specific heat of dry air at constant pressure, and α the proportionality coefficient of SHF to Ts – Ta. As mentioned in section 2a, here we also assume that Ts is almost constant in time due to the large thermal inertia owing to the deep ocean mixed layer and strong advective effects of the mean currents. This assumption is found to be valid in the KOE region. The purpose of this estimation is not to carry out a complete heat budget analysis, but rather to provide a crude estimation of the potential efficiency of the restoration process of the

SAT gradient across the oceanic frontal zone through SHF. At a location to the south of the subarctic front (37°N, 150°E) in the KOE region, typical values for H (=2000 m) and α (=15 W m^{-2} K^{-1}) yield an estimation of τ that is as short as 1.1 day. It is comparable to the estimation by Nonaka et al. (2009) for the southern Indian Ocean frontal zone. Our estimation is also consistent with an indirect estimation of τ through their trajectory analysis for the North Pacific storm track by Swanson and Pierrehumbert (1997), who pointed out for the first time the importance of thermal damping of lower-tropospheric air temperature toward the underlying SST in maintaining

the near-surface baroclinicity. Note that τ becomes even shorter if condensation occurs in the mixed layer as discussed below. Nakamura et al. (2004, 2008) pointed out that this efficient restoration of the SAT gradient across a midlatitude oceanic frontal zone is crucial for the recurrent development of cyclones and anticyclones along a storm track. After the termination of the monsoonal wind, this restoration can operate effectively in spring to act against the relaxing effects of the poleward heat transport associated with synoptic eddies. In fact, Fig. 9f indicates that the springtime axis of the surface baroclinic zone coincides with the axis (41°N) of the subarctic oceanic frontal zone (Fig. 9e).

In winter the surface baroclinic zone (39°~43°N) is slightly weaker and broader than in spring, despite the fact that the meridional gradient of the seasonal-mean SHF across the subarctic frontal zone is 3 times stronger than in spring. This may be attributable to the strong advective effects of the prevailing monsoonal northerly winds across the subarctic frontal zone. In fact, the axis of the surface baroclinic zone (39°N) is shifted onto the equatorward flank of the oceanic frontal zone, located ~2° latitude away from the frontal axis. This displacement seems consistent with the distance (~216 km) over which an air parcel would travel following the mean northerly wind of ~2.5 m s^{-1} simulated over 36°–39°N (Fig. 7a) during the restoration time scale of 1 day (Fig. 9b). Consider an idealized situation where an oceanic front with step-function-like SST distribution extends zonally under northerly winds (e.g., Fig. SB3b in Xie 2004). In this situation, the e-folding downwind distance of the thermally adjusted SAT should be proportional to the northerly wind speed. Thus, the strong wintertime northerly monsoonal winds lead to the weakening of the SAT gradient across the subarctic front, as shown in Fig. 9b.

In addition to the heat exchange with the ocean through SHF, latent heat release associated with low cloud formation, if it happens, could alter the mixed layer heat budget and thereby contribute to either the maintenance or destruction of the meridional SAT gradient. An inspection of meridional sections of the cloud liquid water mixing ratio zonally averaged over the KOE region (not shown) shows that the cloud water in the mixed layer (below the 900-hPa level) increases in the CNTL experiment relative to the SMTH experiment predominantly to the north of the subarctic front both in winter and spring. The increased low-level cloud amount is consistent with the increased (stabilized) near-surface static stability in the presence of the subarctic front (Figs. 4e and 4f). Thus, the effects of the latent heat release associated with the cloud formation in the mixed layer act to deconstruct the cross-frontal SAT gradient,

further suggesting the importance of SHF in maintaining the near-surface baroclinicity.

b. Storm-track activity

It has been established theoretically and observationally that the near-surface baroclinicity is crucial to the baroclinic growth of synoptic disturbances through enhancing the vertical coupling between incoming upper-level eddies and potential vorticity anomalies induced thermally at the surface (e.g., Hoskins et al. 1985; Nakamura and Sampe 2002). We first examine the 850-hPa poleward heat flux associated with synoptic eddies as a measure of their baroclinic growth along the Pacific storm track. In the following analysis, subweekly fluctuations in temperature and the meridional wind velocity associated with transient eddies[4] have been extracted by applying a Lanczos high-pass filter with a half-power cutoff period of 8 days to the daily mean model output. Wintertime and springtime distributions of the eddy heat flux simulated in the CNTL experiment (Figs. 10c and 10d, respectively) compare well over the Pacific with their counterparts based on the JRA-25 analysis (Figs. 10a and 10b, respectively). Though slightly underestimated, the springtime eddy heat flux in the CNTL experiment is concentrated into the storm track located along the subarctic oceanic front (Figs. 9e–g and 10d). As was actually observed by Nakamura (1992), the storm-track activity simulated over the North Pacific weakens in winter (Figs. 9c and 10c) relative to that in spring (Figs. 9g and 10d). The weakening is associated with the seasonal intensification of the upper-tropospheric subtropical jet (Figs. 10a and 11a; Nakamura et al. 2002), whose core is higher and located southward relative to the polar-front jet than was observed (Fig. 10b) and simulated (Fig. 11d) in spring. The CNTL experiment can thus reproduce the midwinter suppression of the North Pacific storm-track activity. Nakamura and Sampe (2002) argued that the trapping of upper-level eddies into the seasonally intensified and southward-displaced subtropical jet core impairs the vertical coupling of the eddies with the surface baroclinic zone anchored along the subarctic oceanic front, leading to less efficient energy conversion for their baroclinic growth.

Both in winter and spring the eddy heat transport is reduced substantially in the SMTH experiment (Figs. 10e and 10f), in which the SAT gradient is relaxed toward the smoothed SST profile (Figs. 9b and 9f), confirming the role of surface baroclinicity in maintaining the lower-tropospheric storm-track activity. The springtime reduction of eddy activity is so marked that the 850-hPa storm

---

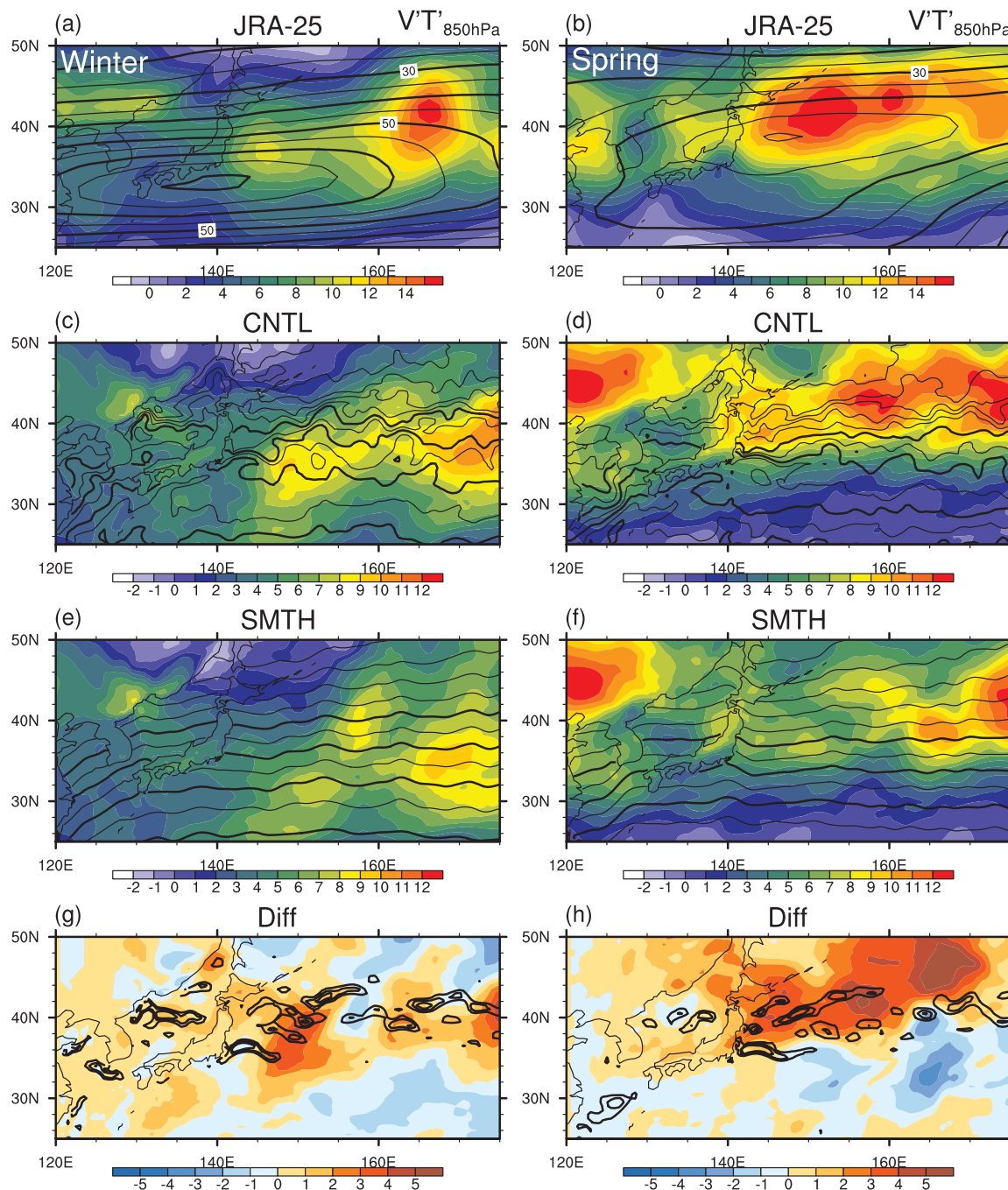[4] Hereafter, transient eddies are referred to as eddies.

FIG. 10. The 850-hPa poleward eddy heat flux $\overline{v'T'}$ (color shading as indicated at the bottom, K m s^{-1}) based on (a),(b) the JRA-25 data, and the (c),(d) CNTL and (e),(f) SMTH experiments, in addition to (g),(h) the difference between the two experiments (CNTL–SMTH). The eddy component has been extracted through high-pass filtering with a half cutoff period of 8 days to the daily mean time series. (a),(b) The seasonal-mean 250-hPa zonal wind speed is superposed with black contours (every 5 m s^{-1}, thickened for every 10 m s^{-1}). (c),(f) The prescribed SST field is superposed with black contours with intervals of 2°C, and the contours for 12°, 16°, 20°, and 24°C are thickened. (g),(h) Mean meridional SST gradients assigned in the CNTL experiment are superposed with black contours for 2°, 3°, and 4°C (100 km)$^{-1}$. Left [(a),(c),(e),(g)] and right [(b),(d),(f),(h)] panels are for winter and spring, respectively.
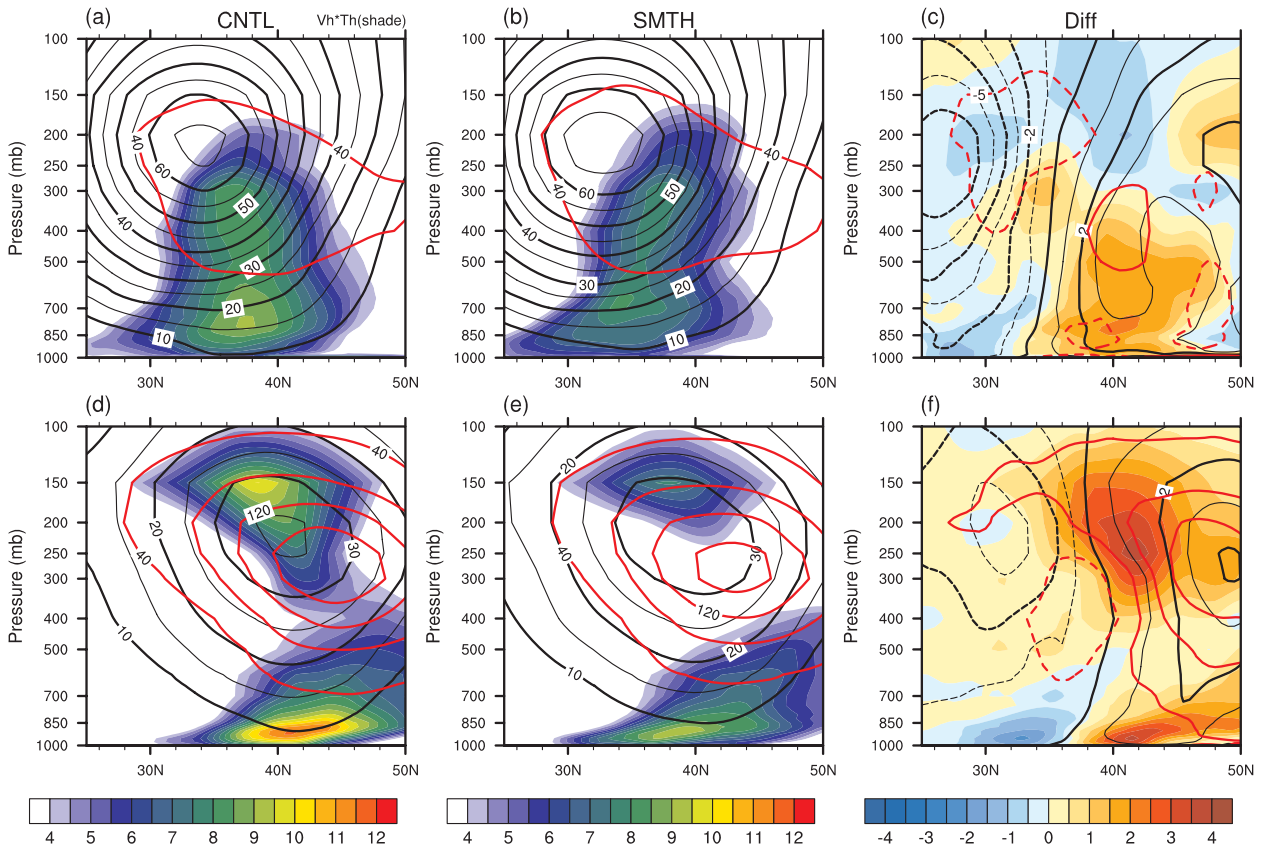
FIG. 11. Meridional sections of poleward eddy heat flux $\overline{v'T'}$ (color shading as indicated at the bottom, K m s^{-1}) and the variance of the meridional wind velocity $\overline{v'^2}$ (red contours with intervals of 40 m^2 s^{-2}) based on zonal averaging over the KOE region (145°E~180°) simulated for winter in the (a) CNTL and (b) SMTH experiments, in addition to (c) their difference [i.e., (a) − (b)]. The corresponding distributions of the mean westerly wind speed are superposed with black contours (every 5 m s^{-1} for the CNTL and SMTH experiments, and every 1 m s^{-1} for their difference; every other contour is thickened, and negative contours are dashed). (d)–(f) Same as in (a)–(c), respectively, but for spring.

track is no longer well defined along the subarctic front off of Japan (Fig. 10f). Figure 11 shows meridional sections of the eddy heat flux (color shading) and the meridional wind variance (red contours) associated with synoptic eddies for the CNTL and SMTH experiments and their differences after being averaged longitudinally over the KOE region (145°E~180°). Relative to the SMTH experiment, the CNTL experiment simulates substantial enhancements and reductions of the springtime eddy heat flux below the 800-hPa level along the subarctic oceanic frontal zone (39°~45°N) and to its south, respectively (Fig. 11f), which can be viewed as the northward shift of the storm-track axis (Figs. 11d and 11e). Along the frontal zone the enhancement of the eddy activity is also substantial at the tropopause level (Fig. 11f), suggestive of the stronger vertical coupling of eddies that leads to their enhanced baroclinic growth. The meridional wind variance associated with the eddies also indicates the enhancement of eddy activity and the northward shift of the storm-track axis at the tropopause

level (Fig. 9h; red contours in Fig. 11f). The two experiments also highlight the significant influence exerted by the frontal SST gradient on the wintertime storm-track activity. Relative to the realistically simulated storm track in the CNTL experiment (Fig. 11a), its axis is displaced equatorward by ~300 km at the 850-hPa level and eddy activity weakens substantially in the SMTH experiment (Fig. 10b). Unlike in spring, the increases in the wintertime eddy heat flux and meridional wind variance are significant only in the lower half of the troposphere (Fig. 11c), consistent with the trapping of upper-level eddies into the subtropical jet core (red contours in Figs. 11a and 11b) and the weaker vertical coupling for baroclinic disturbances in winter (Nakamura and Sampe 2002). It is worthwhile to mention that both in winter and spring the enhanced atmospheric eddy activity along the oceanic frontal zone and the associated enhancement in poleward eddy transport of heat and westerly momentum in the CNTL experiment give rise to stronger westerlies throughout the depth of the

troposphere, including at the surface, around the frontal zone and its poleward side, and weaker westerlies to the south (Figs. 11c and 11f).

In addition to the direct impacts of the increased SST gradients in the subarctic oceanic frontal zones discussed above, the storm track and the jet structure can be modified by the Hadley circulation, which has been shown to be highly sensitive to the SST gradients in the subtropics (Brayshaw et al. 2008). Both in spring and winter, the SST gradients south of 35°N are indeed weaker in the CNTL experiment than in the SMTH experiment (Figs. 9a and 9e). This reduction in the subtropical SST gradients and the associated reduction in the SST difference between the tropics and extratropics could contribute to the weakening of the subtropical jet, which could lead to the dominance of the eddy-driven midlatitude jet. In our experiments, however, the strength of the Hadley cell is constrained by the lateral restoring at the model's southern boundary along 15°N and thus the response of the Hadley cell to the reduced SST gradients is unlikely to make a significant contribution to the simulated storm-track and jet structures.

Our comparison between the CNTL and SMTH experiments extends into the energetics of the synoptic disturbances, to confirm the influence of the frontal SST gradient on the Pacific storm-track activity in winter and spring. Following Kosaka and Nakamura (2006, 2008), we have locally evaluated kinetic energy (EKE = $\frac{1}{2}(u'^2 + v'^2)$) and available potential energy [EAPE = $RT'^2/(2\sigma p)$], which are both associated with synoptic eddies, by using the high-pass-filtered quantities (as denoted with primes). Here, σ denotes the stability parameter $\sigma = R\langle\overline{T}\rangle_{\mathrm{KOE}}/C_p p - \partial\langle\overline{T}\rangle_{\mathrm{KOE}}/\partial p$ for the seasonal-mean state (as denoted by overbars) averaged over the KOE frontal region (35°~55°N, 140°~170°E; denoted as $\langle\rangle_{\mathrm{KOE}}$) and R the gas constant for dry air. The barotropic and baroclinic energy conversions (CK and CP, respectively) from the mean flow to the eddies have also been evaluated locally as follows:

$$\mathrm{CK} = \frac{v'^2 - u'^2}{2}\left(\frac{\partial\overline{u}}{\partial x} - \frac{\partial\overline{v}}{\partial y}\right) - u'v'\left(\frac{\partial\overline{u}}{\partial y} + \frac{\partial\overline{v}}{\partial x}\right)$$

and

$$\mathrm{CP} = -\frac{R}{\sigma p}\left(v'T'\frac{\partial\overline{T}}{\partial y} + u'T'\frac{\partial\overline{T}}{\partial x}\right).$$

Figure 12 compares CP, APE, EKE, and CK between the CNTL and SMTH experiments, each of which has been integrated vertically between the 1000- and 100-hPa levels and then averaged over the spring season. In the CNTL experiment, CP is maximized around the western

portion (140°~160°E) of the subarctic oceanic front (Fig. 12a), where the SST front-induced enhancement of CP is also greatest (Fig. 12k). The CP enhancement is due to increases both in the available potential energy (APE) of the mean state (i.e., enhanced mean temperature gradient) and in the poleward eddy heat flux. Consistently, the maximum of EAPE is located just downstream of the CP maximum (Fig. 12b), and the maximum EKE is situated farther downstream (Fig. 12c). Meanwhile, CK is overall negative within the subarctic frontal zone (Fig. 12d), to accelerate the mean westerlies through the eddy–mean flow interaction. The largest negative CK occurs in the region of the EKE maximum. A series of these energy conversions represents the baroclinic growth of the synoptic disturbances over the western portion of the subarctic front and their subsequent barotropic decay downstream. These energy conversions and the eddy energy are substantially weaker in the SMTH experiment (Figs. 12f–i). Table 1 summarizes the springtime eddy energies averaged both vertically between the 1000 and 100-hPa levels and horizontally over the KOE frontal zone (35°~55°N, 140°E~170°), where the storm-track activity is enhanced substantially due to the frontal SST gradients. Compared to the SMTH experiment, EKE and EAPE, if spatially averaged, both increase by ~11% and ~8%, respectively, in the CNTL experiment, while the increase of the spatially averaged CP is ~23%. In the CNTL experiment, the efficiency of the baroclinic energy conversion measured by CP/(EKE + APE) is thus ~12% higher than in the SMTH experiment. Meanwhile, the negative CK is stronger by as much as 106%, which is suggestive of the critical role of the frontal SST gradient in the formation of the polar-front jet in spring over the North Pacific by energizing storm-track activity, and consistent with the stronger springtime jet in the CNTL experiment (Figs. 11d and 11e).

In contrast, the energetics for synoptic disturbances in winter are not as typical as simulated in spring. Table 2 summarizes the wintertime energetics over the KOE frontal zone as the counterpart to Table 1. The wintertime EKE is ~48% less than that in spring, consistent with weaker storm-track activity in winter than spring (cf. Figs. 10c and 10d and Figs. 11a and 11d). While CP in the CNTL experiment is slightly larger due to higher mean-flow baroclinicity within the entire troposphere, it is only ~5% larger than that in the SMTH experiment. The baroclinic energy conversion rate CP/(EKE + EAPE) increases by ~19% in the CNTL experiment compared to the SMTH experiment, but this seemingly large increase is due to the reduction of the total eddy energy EKE + EAPE. In fact, wintertime reductions in EKE and EAPE from the SMTH to the CNTL experiment are ~13% and ~8%, respectively.
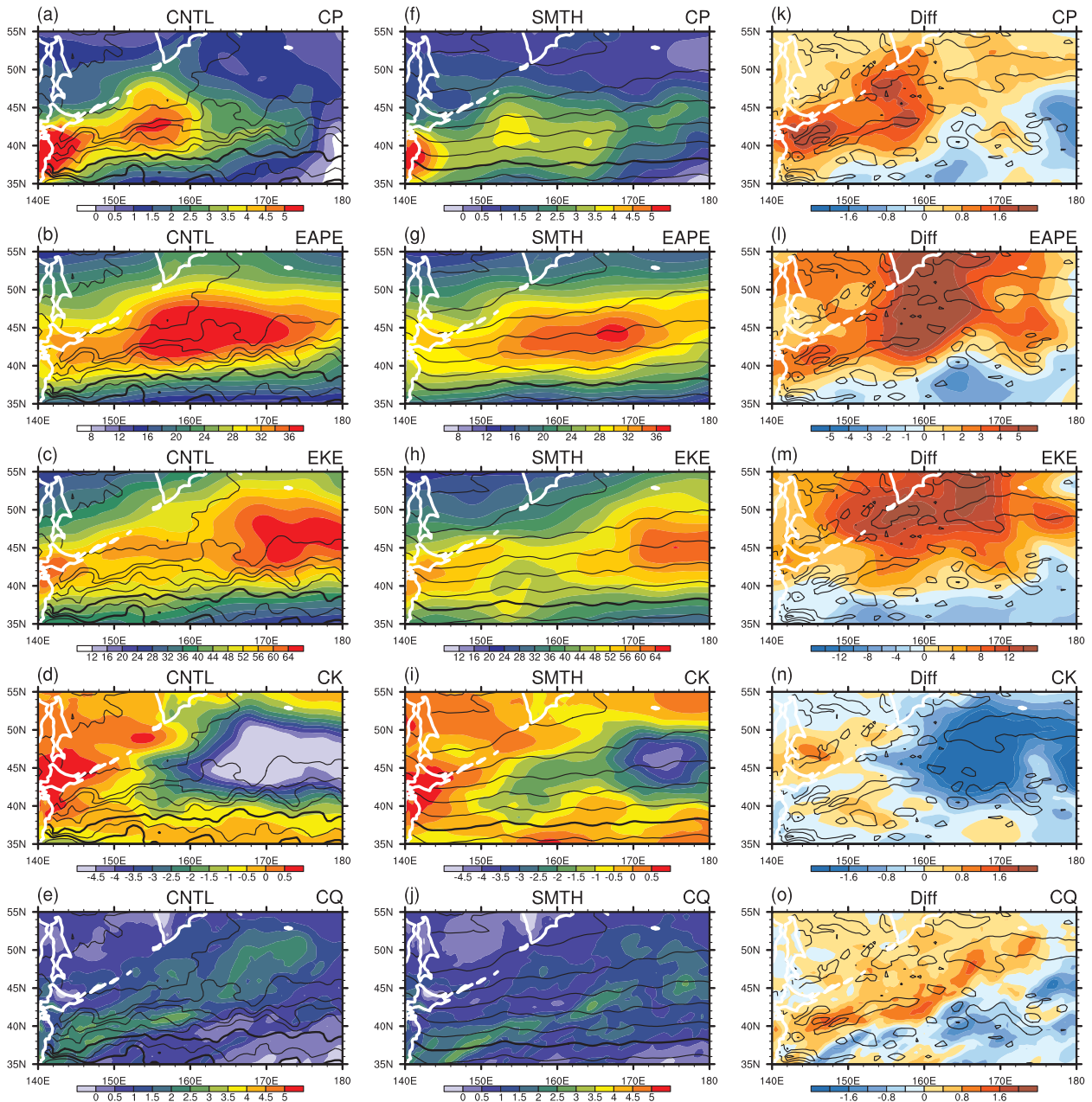
FIG. 12. Vertically averaged energetics for subweekly synoptic-scale eddies simulated in the CNTL experiment for spring (color shading as indicated at the bottom): (a) CP ($\times 10^{-4}$ m^2 s^{-3}), (b) EAPE (m^2 s^{-2}), (c) EKE (m^2 s^{-2}), (d) CK ($\times 10^{-4}$ m^2 s^{-3}), and CQ ($\times 10^{-4}$ m^2 s^{-3}). Mean SST distribution prescribed on the model boundary is superposed with black contours (every 2°C; thickened for 12° and 16°C). (f)–(j) Same as in (a)–(e), respectively, but for the SMTH experiment. (k)–(o) Same as in (a)–(e), respectively, but the differences between the CNTL and SMTH experiments (CNTL–SMTH). The mean meridional SST gradient assigned for the CNTL experiment is superposed with black contours for 2°, 3°, and 4°C (100 km)$^{-1}$.

In summary, our regional model experiments suggest that, though confined to a zonal sector (140°E~180°), a sharp SST gradient in the KOE region and its maintenance of near-surface baroclinicity can exert a significant thermal impact on the large-scale circulation of the overlying atmosphere by energizing and anchoring the storm track, especially in spring. Our results are consistent with numerical experiments by Nakamura et al. (2008), which revealed the importance of midlatitude frontal SST gradients for the maintenance of midlatitude storm-track activity and a deep westerly jet (polar front jet). Our results are also consistent with

TABLE 1. Springtime energetics associated with synoptic eddies simulated in the CNTL and SMTH experiments on the basis of vertical (between the 1000- and 100-hPa levels) and horizontal averaging over the subpolar frontal region (35°–55°N, 140°–170°E). Evaluation has been made for EKE and EAPE ($m^2 s^{-2}$); CK, CP, and CQ ($\times 10^{-4} m^2 s^{-3}$); and energy conversion rates ($\times 10^{-6} s^{-1}$) defined as CP/(EKE + APE) and CQ/(EKE + APE). A positive (negative) value of the energy conversion means energy gain (lose) for eddies from (to) the seasonal mean state.

	EKE	APE	CK	CP	CQ	CP/(EKE + APE)	CQ/(EKE + APE)
CNTL	47.64	27.91	−1.04	2.66	1.25	3.52	1.65
SMTH	42.98	25.77	−0.51	2.17	1.10	3.16	1.60

Kobashi et al. (2008), who recently found that meso-α-scale cyclones are energized baroclinically along the North Pacific subtropical front.

6. Moist processes

Several studies have emphasized the importance of the moisture supply from warm ocean currents and latent heat release associated with precipitation in energizing the storm-track activity (Hoskins and Valdes 1990; Inatsu et al. 2003; Minobe et al. 2008). The moist processes are important for the amplification of individual cyclones (e.g., Kuo et al. 1991; Kuwano-Yoshida and Asuma 2008), since their heat exchanges with the underlying ocean via SHF, on one hand, acts to restore the SAT gradient but, on the other hand, it acts as thermal damping for SAT anomalies associated with them (Nakamura et al. 2004). In this section, we discuss the relationship between LHF, precipitation, and storm activity in our simulations.

a. Signature of oceanic fronts on LHF and precipitation

Figure 13 compares the precipitation rates between the CNTL experiment and the GPCP analysis. Though somewhat overestimated, the model captures salient features of the observed precipitation pattern, including a well-defined zonal band of wintertime precipitation maximum around 38°N east of 150°E along the storm track, and two precipitation maxima in spring, one extending zonally along the subarctic front east of 145°E and the other located downstream of an SST front along the continental shelf over the East China Sea. Relative to the SMTH experiment, all these three features manifest themselves as notable increases in precipitation along the warm currents and/or associated oceanic fronts (Figs. 13c and 13d), suggestive of their impact.

Major factors for the enhanced precipitation rate include enhanced storm-track activity and increased local evaporation from the ocean along the (not necessarily enhanced) storm track (passage of synoptic disturbances). Both in winter and spring the precipitation increase to the east of Japan is attributable to enhanced evaporation along the KE (Figs. 3g and 3h) and the resultant increase in the moisture supply to cyclones developing along the storm track. The cyclone development itself tends to be enhanced (Fig. 10) due to the enhanced SAT gradient across the subarctic frontal zone (Fig. 8). In spring, no significant enhancement in storm-track activity is simulated over the East China Sea and south of Japan along the Kuroshio (Fig. 10h), where the precipitation increase in the CNTL experiment is primarily due to a direct contribution from locally enhanced evaporation over the warm band of SST (Figs. 3d and 3h).

b. Contribution of diabatic heating on storm-track energetics

The horizontal distributions of the simulated latent heating rate due to the atmospheric convection and large-scale condensation vertically averaged between the 1000- and 100-hPa levels is quite similar to that of the precipitation rate, with the maximum heating rate reaching up to 2 K day^{-1} along the warm ocean currents (not shown). The oceanic frontal signatures on the latent heating rate are characterized by confinement of the heating regions along the warm Kuroshio Current south of Japan and the KE front to the east, and their northward shift in the CNTL experiment due to the presence of the oceanic fronts. How important is such diabatic heating in energizing the eddy activity along the storm track? To address this question, we estimate the APE generation due to the diabatic heating as

TABLE 2. Same as in Table 1 but for wintertime energetics.

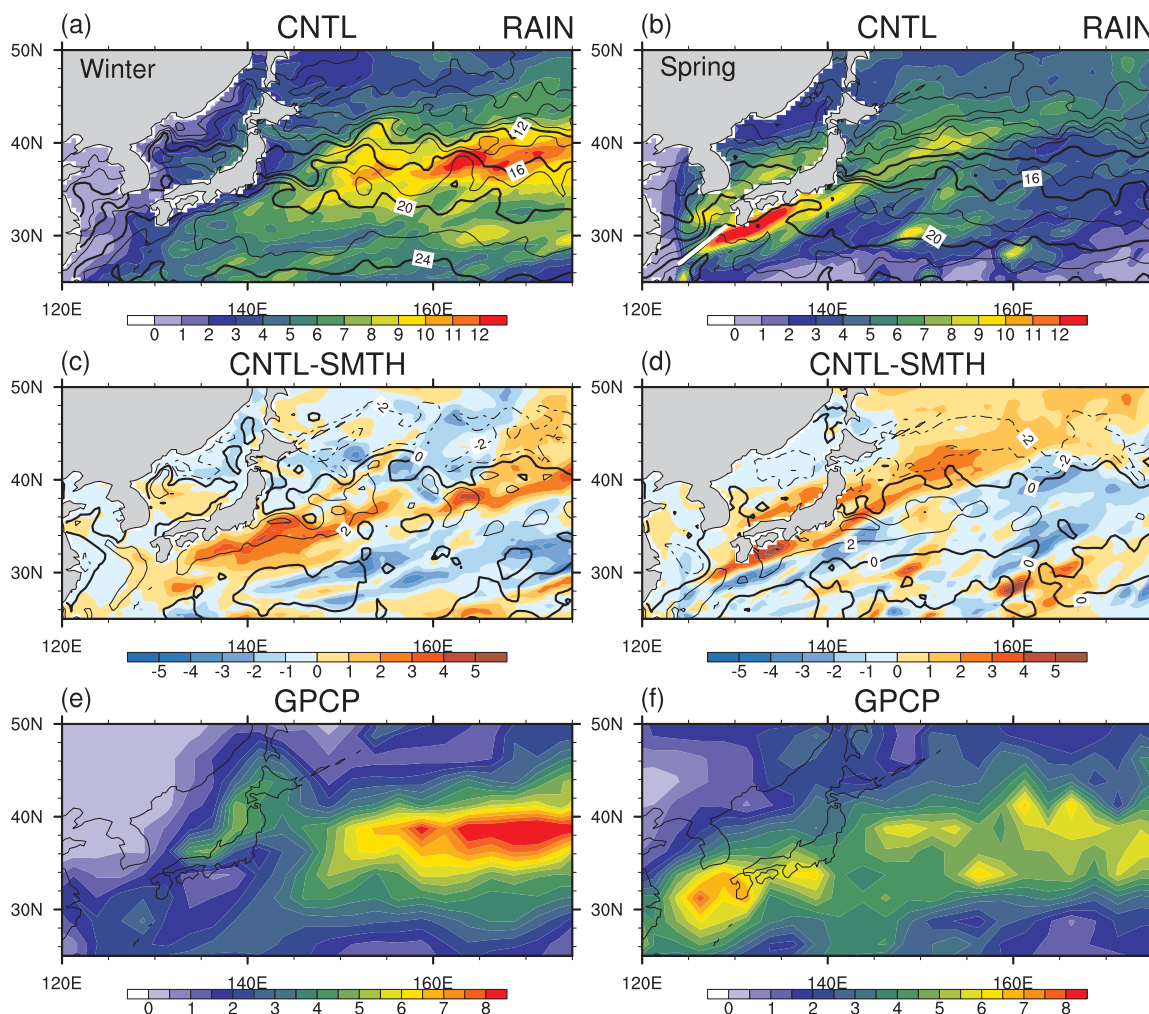|	EKE	APE	CK	CP	CQ	CP/(EKE + APE)	CQ/(EKE + APE)
CNTL	24.85	16.72	0.31	2.69	1.06	6.46	2.55
SMTH	28.63	18.26	0.18	2.55	1.45	5.44	3.10

FIG. 13. Mean precipitation (color shading as indicated at the bottom, mm day^{-1}) simulated in the CNTL experiment for (a) winter and (b) spring. The mean SST distribution prescribed at the model boundary is superposed with black contours (every 2°C; thickened for 12°, 16°, 20°, and 24°C). In (b), an SST front along the continental shelf break of the East China Sea is indicated with a thick white line. (c),(d) Same as in (a),(b), respectively, but for the differences in precipitation (color) and SST (contoured for every 2°C; dashed for negative values) between the CNTL and SMTH experiments. (e),(f) Same as in (a),(b), respectively, but precipitation based on the GPCP analysis.

$$CQ = \frac{(R/C_p)\overline{T'Q'}}{p\sigma},$$

where Q' is the total diabatic heating that includes the latent heat release due to the atmospheric convection and large-scale condensation as well as the heating due to radiative and subgrid-scale mixing/diffusion processes. One way to measure the relative importance of the moist processes in the storm-track activity is to compare the diabatic APE generation (CQ) with the baroclinic energy conversion (CP) with respect to their efficiencies in generating eddy energies. In the CNTL experiment for spring, the vertically averaged CQ between the 1000- and 100-hPa levels is more strongly confined in the

meridional direction than the vertically averaged CP (cf. Figs. 12a and 12e), and its maximum value is about half of its counterpart of CP. For a quantitative comparison, the same KOE frontal region is chosen for the spatial and vertical averaging as in section 5b (Tables 1 and 2). In the CNTL experiment in spring (winter), the horizontally averaged CQ amounts to ~47% (40%) of its counterpart for CP. Compared to the SMTH experiment, the horizontal-mean CQ in the CNTL experiment increases by ~13% in spring, whereas it decreases by ~27% in winter. As far as the efficiency of the energy conversion/generation in the CNTL experiment is concerned, the contribution of moist processes to the baroclinic growth of synoptic disturbances over the KOE frontal region [CQ/(APE + EKE)] accounts for ~47%

and ~40% in spring and winter, respectively, of that of the dry processes [CP/(APE + EKE)].

In the KOE frontal region, there may be interactions between the storm-track activity and SST through the formation of low-level stratus clouds, which is sensitive to the underlying SST that controls the near-surface static stability. The high albedo of those clouds acts to lower SST, thereby increasing the static stability. This cloud–SST feedback is most likely to be operative in summer (e.g., Norris et al. 1998). To focus on the oceanic influence on the storm-track activity, however, we purposely exclude the cloud radiative impacts on SST in the present study by prescribing the SST as the lower boundary condition of the model. This impact should be addressed with an ocean–atmosphere coupled model in our future study.

7. Summary and discussion

In the present study, the influence of SST fronts in the KOE region on surface turbulent heat fluxes and the overlying atmosphere has been investigated by means of atmospheric regional model experiments for the 2003/04 cold season. Our primary focus on the maintenance of surface baroclinicity and its influence on the lower-tropospheric storm-track activity. A pair of experiments, one with frontal SST structures resolved in the model boundary condition and the other without them, highlights the confinement and intensification of surface SHF and LHF around narrow oceanic fronts in the KOE region. In the CNTL experiment only, distinctive air–sea heat exchanges are simulated across an oceanic front that are favorable for restoring the cross-frontal SAT gradient effectively for recurrent development of cyclones and anticyclones to counteract the relaxing effects of eddy poleward heat transport. The present study, Nonaka et al. (2009), and Sampe et al. (2010, hereafter SNGO) indicate that the SHF-induced restoration of frontal SAT gradient, which may be called oceanic baroclinic adjustment (Nakamura et al. 2008), is particularly effective if associated with migratory atmospheric disturbances. Traveling along the oceanic front, the disturbances induce warm- and cold-air advection across it, which relaxes the SAT gradient and augments the positive and negative SST − SAT differences (i.e., surface static stability) on the warmer and cooler sides of the front, respectively. After being relaxed by atmospheric disturbances, the cross-frontal SAT gradient can be restored efficiently within 1~2 days by temporarily enhanced SHF upward and downward on the warmer and cooler sides of the frontal zone, respectively. Reflecting this temporary nature of SHF and its restoring effects on the SAT gradient along the storm track, the sign reversal can be seen across the oceanic front not only in the seasonal mean field of SHF but also in its skewness field. Our CNTL experiment simulates the lower-tropospheric storm-track activity over the KOE region in a realistic manner both in winter and spring, while the activity is reduced by 15%~20% and the storm-track axis is unrealistically displaced equatorward in the SMTH experiment, where frontal SST signatures are smoothed out in the model boundary condition. In the CNTL experiment the enhancement in eddy activity and evaporation on the warmer side of the front leads to an increase in precipitation along the storm track. Our analysis of the energetics confirms that in both winter and spring eddy energies are more efficiently converted from the mean state in the CNTL experiment than in the SMTH experiment. Though to a less degree, the diabatic heating associated with moist processes also contributes substantially to the generation of eddy energies. Though limited to a single cold season and not based on ensemble integrations, our model experiments suggest that a sharp oceanic front, limited zonally as in the KOE region, can anchor a storm track along it by energizing atmospheric eddies, as suggested from the atmospheric reanalysis (Nakamura et al. 2004) and idealized aquaplanet-type AGCM experiments (Nakamura et al. 2008; Brayshaw et al. 2008; SNGO).

Our experiments also realistically simulate winter–spring differences in the heat flux distribution. Unlike spring when the large-scale pattern of the surface heat fluxes is determined by recurrent passages of synoptic disturbances, the pattern is determined primarily by monsoonal northwesterlies from the Eurasian continent in winter. On top of this large-scale pattern, imprints of the oceanic fronts are superimposed. As in spring, the mean SHF and LHF in winter exhibit sharp gradients across the oceanic fronts, around which the variability of the fluxes is elevated. The enhanced variability is due to the enhanced storm-track variability along the fronts where the mean meridional SAT gradient is augmented. Nevertheless, some of these features in SHF are subject to modifications under the persistent monsoonal wind. Unlike spring, for example, the wintertime SHF skewness does not exhibit sign reversal across the oceanic fronts. Furthermore, despite the sharp cross-frontal gradient in the winter-mean SHF, which acts to maintain the SAT gradient locally, the winter-mean SAT gradient east of Japan is weaker and shifted slightly equatorward due to the advective effects of the monsoonal wind.

Our numerical results have some implications for the North Pacific climate and its interannual to decadal variability documented in previous observational studies. Nakamura and Sampe (2002) discussed decadal changes of the winter storm-track activity over the western North

Pacific in relation to the strength of the subtropical jet and its trapping effects of upper-level eddies into the jet core away from a surface baroclinic zone around 40°N anchored along oceanic fronts. Analyzing their own surface heat flux data based on in situ ship measurements, Tanimoto et al. (2003) argued that decadal SST changes in the North Pacific subarctic frontal zone may modify the heat supply from the ocean to influence storm-track activity, which may reinforce the anomalous intensity of the Aleutian low through anomalous convergence of eddy vorticity flux. Our regional model experiments have confirmed the importance of the oceanic frontal zone in the KOE region in maintaining the surface baroclinic zone via cross-frontal contrasts in SHF (i.e., oceanic baroclinic adjustment) to retain storm-track activity as observed. The atmospheric response extracted from our experiments is likely to overestimate the response that would, if any, be induced by observed interannual or decadal changes in the strength of the oceanic fronts, because we artificially imposed rather intense smoothing on the SST field in the SMTH experiment. Nevertheless, the present study provides a qualitative basis for a better understanding of the role of the oceanic fronts on the mean state of the atmospheric circulation and its response to more realistic interannual to decadal changes in oceanic fronts that include their meridional shift. Studies are emerging that suggest the potentially important impacts of the oceanic fronts on the mean state of the extratropical atmosphere and the interannual to decadal-scale climate variability. A set of AGCM experiments by Nakamura et al. (2008) suggests the potential importance of midlatitude oceanic frontal zones in maintaining storm-track activity and eddy-driven polar front jets, whose variability is regarded as the annular modes. Analyzing an atmospheric reanalysis dataset, Nakamura and Yamane (2009) showed close associations on interannual time scales among the near-surface baroclinicity, atmospheric mean flow, and storm track in the North Atlantic basin. Using a linear moist baroclinic model, Minobe et al. (2008) have suggested the possible downstream influence of a prescribed deep diabatic heating pattern along the Gulf Stream. Quantitative assessment of the significance of the oceanic influence on the large-scale atmospheric circulation and its variability over the North Pacific and other midlatitude ocean basins calls for further studies, for example, through performing ensemble experiments with a high-resolution AGCM, a regional model, or a coupled GCM, in any of which the horizontal resolution must be sufficient for resolving narrow oceanic frontal zones.

REFERENCES

Brayshaw, D., B. J. Hoskins, and M. J. Blackburn, 2008: The storm-track response to idealized SST perturbations in an aquaplanet GCM. *J. Atmos. Sci.,* **65,** 2842–2860.

Chelton, D. B., M. G. Schlax, M. H. Freilich, and R. F. Milliff, 2004: Satellite measurements reveal persistent small-scale features in ocean winds. *Science,* **303,** 978–983.

Fairall, C., E. Bradley, J. Hare, A. Grachev, and J. Edson, 2003: Bulk parameterization of air–sea fluxes: Updates and verification for the COARE algorithm. *J. Climate,* **16,** 571–591.

Hoskins, B., and P. J. Valdes, 1990: On the existence of storm tracks. *J. Atmos. Sci.,* **47,** 1854–1864.

——, M. E. McIntyre, and A. Robertson, 1985: On the use and significance of isentropic potential vorticity maps. *Quart. J. Roy. Meteor. Soc.,* **111,** 877–946.

Huffman, G., R. Adler, M. Morrissey, D. Bolvin, S. Curtis, R. Joyce, B. McGavock, and J. Susskind, 2001: Global precipitation at one-degree daily resolution from multisatellite observations. *J. Hydrometeor.,* **2,** 36–50.

Inatsu, M., H. Mukougawa, and S.-P. Xie, 2003: Atmospheric response to zonal variations in midlatitude SST: Transient and stationary eddies and their feedback. *J. Climate,* **16,** 3314–3329.

Kako, S., and M. Kubota, 2007: Variability of mixed layer depth in Kuroshio/Oyashio Extension region: 2005–2006. *Geophys. Res. Lett.,* **34,** L11612, doi:10.1029/2007GL030362.

Kalnay, E., and Coauthors, 1996: The NCEP/NCAR 40-Year Reanalysis Project. *Bull. Amer. Meteor. Soc.,* **77,** 437–471.

Kelly, K., and S. Dong, 2004: The relationship of western boundary current heat transport and storage to midlatitude

ocean–atmosphere interaction. *Earth's Climate: The Ocean–Atmosphere Interaction, Geophys. Monogr.,* Vol. 147, Amer. Geophys. Union, 347–363.

Kobashi, F., S.-P. Xie, N. Iwasaka, and T. Sakamoto, 2008: Deep atmospheric response to the North Pacific oceanic subtropical front in spring. *J. Climate, 21,* 5960–5975.

Kosaka, Y., and H. Nakamura, 2006: Structure and dynamics of the summertime Pacific–Japan (PJ) teleconnection pattern. *Quart. J. Roy. Meteor. Soc., 132,* 2009–2030.

——, and ——, 2008: A comparative study on the dynamics of the Pacific–Japan (PJ) teleconnection pattern based on reanalysis datasets. *Sci. Online Lett. Atmos., 4,* 9–12.

Kubota, M., and H. Tomita, 2007: Present state of the J-OFURO air–sea interaction data product. *Flux News, 4,* 13–15.

Kuo, Y.-H., R. J. Reed, and S. Low-Nam, 1991: Effects of surface energy fluxes during the early development and rapid intensification stages of seven explosive cyclones in the western Atlantic. *Mon. Wea. Rev., 119,* 457–476.

Kushnir, Y., W. A. Robinson, I. Bradé, N. M. J. Hall, S. Peng, and R. Sutton, 2002: Atmospheric GCM response to extratropical SST anomalies: Synthesis and evaluation. *J. Climate, 15,* 2233–2256.

Kuwano-Yoshida, A., and Y. Asuma, 2008: Numerical study of explosively developing extratropical cyclones in the northwestern Pacific region. *Mon. Wea. Rev., 136,* 712–740.

Kwon, Y.-O., and C. Deser, 2007: North Pacific decadal variability in the Community Climate System Model version 2. *J. Climate, 20,* 2416–2433.

Langland, R., and C.-S. Liou, 1996: Implementation of an *E–ε* parameterization of vertical subgrid-scale mixing in a regional model. *Mon. Wea. Rev., 124,* 905–918.

Minobe, S., A. Kuwano-Yoshida, N. Komori, S.-P. Xie, and R. Small, 2008: Influence of the Gulf Stream on the troposphere. *Nature, 452,* 206–209.

Nakamura, H., 1992: Midwinter suppression of baroclinic wave activity in the Pacific. *J. Atmos. Sci., 49,* 1629–1641.

——, and J. M. Wallace, 1991: Skewness of low-frequency fluctuations in the tropospheric circulation during the Northern Hemisphere winter. *J. Atmos. Sci., 48,* 1441–1448.

——, and T. Sampe, 2002: Trapping of synoptic-scale disturbances into the North Pacific subtropical jet core in midwinter. *Geophys. Res. Lett., 29,* 1761, doi:10.1029/2002GL015535.

——, and A. S. Kazmin, 2003: Decadal change in the North Pacific oceanic frontal zones as revealed in ship and satellite observation. *J. Geophys. Res., 108,* 3078, doi:10.1029/1999JC000085.

——, G. Lin, and T. Yamagata, 1997: Decadal climate variability in the North Pacific during the recent decades. *Bull. Amer. Meteor. Soc., 78,* 2215–2225.

——, T. Izumi, and T. Sampe, 2002: Interannual and decadal modulations recently observed in the Pacific storm track activity and East Asian winter monsoon. *J. Climate, 15,* 1855–1874.

——, T. Sampe, Y. Tanimoto, and A. Shimpo, 2004: Observed associations among storm tracks, jet streams, and midlatitude oceanic fronts. *Earth's Climate: The Ocean–Atmosphere Interaction, Geophys. Monogr.,* Vol. 147, Amer. Geophys. Union, 329–345.

——, ——, A. Goto, W. Ohfuchi, and S.-P. Xie, 2008: On the importance of mid-latitude oceanic frontal zones for the mean state and dominant variability in the tropospheric circulation. *Geophys. Res. Lett., 35,* L15709, doi:10.1029/2008GL034010.

Nakamura, M., and S. Yamane, 2009: Dominant anomaly patterns in the near-surface baroclinicity and accompanying anomalies in the atmosphere and the oceans. Part I: North Atlantic basin. *J. Climate, 22,* 880–904.

Ninomiya, K., T. Nishimura, T. Suzuki, and S. Matsumura, 2006: Polar-air outbreak and air-mass transformation over the east coast of Asia as simulated by an AGCM. *J. Meteor. Soc. Japan, 84,* 47–68.

Nonaka, M., and S.-P. Xie, 2003: Covariations of sea surface temperature and wind over the Kuroshio and its extension: Evidence for ocean-to-atmospheric feedback. *J. Climate, 16,* 1404–1413.

——, H. Nakamura, Y. Tanimoto, T. Kagimoto, and H. Sasaki, 2006: Decadal variability in the Kuroshio–Oyashio Extension simulated in an eddy-resolving OGCM. *J. Climate, 19,* 1970–1989.

——, ——, ——, ——, and ——, 2008: Interannual-to-decadal variability in the Oyashio Current and its influence on temperature in the subarctic frontal zone: An eddy-resolving OGCM simulation. *J. Climate, 21,* 6283–6303.

——, ——, B. Taguchi, N. Komori, A. Y. Kuwano-Yoshida, and K. Takaya, 2009: Air–sea heat exchanges characteristic of a prominent midlatitude oceanic front in the South Indian Ocean as simulated in a high-resolution coupled GCM. *J. Climate, 22,* 6742–6762.

Norris, J. R., Y. Zhang, and J. M. Wallace, 1998: Role of low clouds in summertime atmosphere–ocean interactions over the North Pacific. *J. Climate, 16,* 1404–1413.

Onogi, K., and Coauthors, 2007: The JRA-25 reanalysis. *J. Meteor. Soc. Japan, 85,* 369–432.

Peng, S., and J. S. Whitaker, 1999: Mechanisms determining the atmospheric response to midlatitude SST anomalies. *J. Climate, 12,* 1393–1408.

Qiu, B., 2000: Interannual variability of the Kuroshio Extension system and its impact on the wintertime SST field. *J. Phys. Oceanogr., 30,* 1486–1502.

——, 2002: The Kuroshio extension system: Its large-scale variability and role in the midlatitude ocean–atmosphere interaction. *J. Oceanogr., 58,* 57–75.

——, 2003: Kuroshio Extension variability and forcing of the Pacific decadal oscillations: Responses and potential feedback. *J. Phys. Oceanogr., 33,* 2465–2482.

——, and S. Chen, 2005: Variability of the Kuroshio Extension jet, recirculation gyre, and mesoscale eddies on decadal timescales. *J. Phys. Oceanogr., 35,* 2090–2103.

——, N. Schneider, and S. Chen, 2007: Coupled decadal variability in the North Pacific: An observationally constrained idealized model. *J. Climate, 20,* 3602–3620.

Sampe, T., H. Nakamura, A. Goto, and W. Ohfuchi, 2010: Significance of a midlatitude SST frontal zone in the formation of a storm track and an eddy-driven westerly jet. *J. Climate,* in press.

Schneider, N., and A. J. Miller, 2001: Predicting western North Pacific Ocean climate. *J. Climate, 14,* 3997–4002.

——, and B. D. Cornuelle, 2005: The forcing of the Pacific decadal oscillation. *J. Climate, 18,* 4355–4373.

Scott, R. B., and B. Qiu, 2003: Predictability of SST in a stochastic climate model and its application to the Kuroshio Extension region. *J. Climate, 16,* 312–322.

Seager, R., Y. Kushnir, N. H. Naik, M. A. Cane, and J. Miller, 2001: Wind-driven shifts in the latitude of the Kuroshio–Oyashio Extension and generation of SST anomalies on decadal time scales. *J. Climate, 14,* 4249–4265.

Small, R. J., S.-P. Xie, and Y. Wang, 2003: Numerical simulation of atmospheric response to Pacific tropical instability waves. *J. Climate, 16,* 3723–3741.

——, and Coauthors, 2008: Air–sea interaction over ocean fronts and eddies. *Dyn. Ocean. Atmos., 45,* 274–319.

Swanson, K. L., and R. T. Pierrehumbert, 1997: Lower-tropospheric heat transport in the Pacific storm track. *J. Atmos. Sci.,* **54,** 1533–1543.

Taguchi, B., 2006: A modeling study of the Kuroshio Extension: Decadal variability and influence on the atmosphere. Ph.D. thesis, University of Hawaii at Manoa, 97 pp.

——, S.-P. Xie, N. Schneider, M. Nonaka, H. Sasaki, and Y. Sasai, 2007: Decadal variability of the Kuroshio Extension: Observations and an eddy-resolving model hindcast. *J. Climate,* **20,** 2357–2377.

Tanimoto, Y., H. Nakamura, T. Kagimoto, and S. Yamane, 2003: An active role of extratropical sea surface temperature anomalies in determining anomalous turbulent heat fluxes. *J. Geophys. Res.,* **108,** 3304, doi:10.1029/2002JC001750.

Tokinaga, H., and Coauthors, 2006: Atmospheric sounding over the winter Kuroshio Extension: Effect of surface stability on atmospheric boundary layer structure. *Geophys. Res. Lett.,* **33,** L04703, doi:10.1029/2005GL025102.

——, Y. Tanimoto, S.-P. Xie, T. Sampe, H. Tomita, and H. Ichikawa, 2009: Ocean frontal effects on the vertical development of clouds over the western North Pacific: In situ and satellite observations. *J. Climate,* **22,** 4241–4260.

Tomita, T., S.-P. Xie, and M. Nonaka, 2002: Estimates of surface and subsurface forcing for decadal sea surface temperature variability in the mid-latitude North Pacific. *J. Meteor. Soc. Japan,* **80,** 1289–1300.

Vivier, F., K. Kelly, and L. Thompson, 2002: Heat budget in the Kuroshio Extension region: 1993–99. *J. Phys. Oceanogr.,* **32,** 3436–3454.

Wang, Y., O. L. Sen, and B. Wang, 2003: A highly resolved regional climate model (IPRC-RegCM) and its simulation of the 1998 severe precipitation event over China. Part I: Model description and verification of simulation. *J. Climate,* **16,** 1721–1738.

——, S.-P. Xie, B. Wang, and H. Xue, 2005: Large-scale atmospheric forcing by southeast Pacific boundary layer clouds: A regional model study. *J. Climate,* **18,** 934–951.

Wentz, F. J., and T. Meissner, 2000: Algorithm Technical Basis Document (ATBD) version 2: AMSR ocean algorithm. Remote Sensing Systems Tech. Rep. 121599A, 59 pp.

Xie, S.-P., 2004: Satellite observations of cool ocean–atmosphere interaction. *Bull. Amer. Meteor. Soc.,* **85,** 195–208.

——, T. Kunitani, A. Kubokawa, M. Nonaka, and S. Hosoda, 2000: Interdecadal thermocline variability in the North Pacific for 1958–97: A GCM simulation. *J. Phys. Oceanogr.,* **30,** 2798–2813.

Yasuda, I., K. Okuda, and Y. Shimizu, 1996: Distribution and modification of North Pacific intermediate water in the Kuroshio–Oyashio interfrontal zone. *J. Phys. Oceanogr.,* **26,** 448–465.